Modeling study of turbulent mixing over the continental shelf: Comparison of turbulent closure schemes

H. W. Wijesekera, J. S. Allen, and P. A. Newberger

College of Oceanic and Atmospheric Sciences, Oregon State University, Corvallis, Oregon, USA

Received 27 November 2001; revised 26 September 2002; accepted 4 November 2002; published 29 March 2003.

[1] The sensitivity of model-produced time-dependent wind-driven circulation on the continental shelf to the turbulent closure scheme employed is studied with a two-dimensional approximation (variations across-shelf and in depth) using the Princeton Ocean Model. The level 2.5 Mellor-Yamada closure (MY), k-ε closure, and K-Profile Parameterization schemes are used to evaluate the mesoscale fields and the spatial and temporal variability of mixing. All three submodels produce similar features in the mesoscale circulation. They produce qualitatively similar eddy diffusivities and eddy viscosities, although the turbulent structure and the mixing intensities can differ quantitatively. The k-ε length scale follows the buoyancy length scale when stratification is important. In contrast, the length scale produced by the q^2l equation in the MY scheme deviates substantially from the buoyancy scale unless a stratification-dependent limitation is imposed. During upwelling-favorable winds, the majority of turbulent mixing occurs in the top and the bottom boundary layers and in the vicinity of the vertically and horizontally sheared coastal jet. Turbulent mixing in the coastal jet is primarily driven by shear-production. The near-surface flow on the inner shelf becomes convectively unstable as wind stress forces the upwelled water to flow offshore in the surface layer. During downwelling-favorable winds, the strongest mixing occurs in the vicinity of the downwelling front. The largest turbulent kinetic energy and dissipation are found near the bottom of the front. Turbulence in the bottom boundary layer offshore of the front is concentrated between recirculation cells which are generated as a result of symmetric instabilities in the boundary layer flow. *INDEX TERMS:* 4219 Oceanography: General: Continental shelf processes; 4568 Oceanography: Physical: Turbulence, diffusion, and mixing processes; 4255 Oceanography: General: Numerical modeling; 4279 Oceanography: General: Upwelling and convergences; *KEYWORDS:* numerical modeling, turbulent closure, shelf circulation, turbulent mixing over the shelf

Citation: Wijesekera, H. W., J. S. Allen, and P. A. Newberger, Modeling study of turbulent mixing over the continental shelf: Comparison of turbulent closure schemes, *J. Geophys. Res.*, *108*(C3), 3103, doi:10.1029/2001JC001234, 2003.

1. Introduction

[2] Recent modeling studies by *Allen et al.* [1995] and *Allen and Newberger* [1996] examine the time-dependent response of the coastal ocean to upwelling- and downwelling-favorable winds. Using bathymetry and stratification from the central Oregon shelf, they investigate the development and structure of both upwelling and downwelling density fronts and the accompanying alongshore jets. Both studies use a two-dimensional (i.e., spatial variations across shelf and with depth, uniformity alongshore) version of the Princeton Ocean Model (POM) [*Blumberg and Mellor*, 1987]. *Allen et al.* [1995] find that under constant upwelling-favorable wind forcing a surface density front forms and moves offshore, roughly consistent with existing descriptions of coastal upwelling [e.g., *Brink*, 1983; *Huyer*, 1983]. They also find that the turbulent closure scheme used has substantial impact on the shelf circulation. *Allen and Newberger* [1996] investigate the response to downwelling-favorable winds and also find that the turbulent closure scheme has a significant influence on model-produced downwelling circulation over the shelf.

[3] Direct comparisons of model results for mesoscale velocity and density fields and observations from the Oregon shelf have been made by *Federiuk and Allen* [1995] and *Oke et al.* [2002a, 2002b]. Utilizing POM with a two-dimensional approximation, *Federiuk and Allen* [1995] conduct a 60-day simulation of flow on the Oregon shelf during summer 1973 with realistic bottom topography and initial conditions and with forcing by measured wind stress and buoyancy flux. Model results are compared with current and hydrographic measurements from the Coastal Upwelling Experiment CUE-2. Reasonable agreement of model and observed alongshore velocities is obtained and the qualitative nature of the shelf circulation appears to be well represented, but quantitative differences exist. In work by *Oke et al.* [2002a, 2002b] a three-dimensional simulation of flow on the Oregon shelf, including the region studied by *Federiuk and Allen* [1995] is pursued for 60 days during

0148-0227/03/2001JC001234$09.00

summer 1999 also using POM and comparing model results with measurements from the OSU National Oceanographic Partnership Program (NOPP) field experiment. Overall, encouraging agreement between model results for the mesoscale fields and observations is obtained. For example, model horizontal velocities and temperatures are highly correlated with corresponding observed velocities and temperatures from an inner shelf mooring in 50 m water depth (Figure 1). Similar comparisons at a midshelf mooring in 80 m water depth are not quite as close although time-dependent model density fields show good agreement with repeated hydrographic measurements along an across-shelf section [*Oke et al.*, 2002a].

[4] It is clear that physical circulation models have the potential to represent complex aspects of the wind-driven flows on continental shelves. The fact, however, that the mesoscale flow fields produced by shelf circulation models can depend on the turbulence closure scheme provides a strong incentive for further study of the effectiveness of parameterization methods for small-scale turbulent processes. Definitive model-data comparisons to evaluate the parameterizations are clearly an ultimate objective. Some successes in that regard have been achieved from the analysis of small-scale turbulence measurements in tidally forced situations where reasonable simplifying assumptions about the nature of the large-scale flow could be made [e.g., *Simpson et al.*, 1996; *Burchard et al.*, 1998; *Stacey et al.*, 1999; *Lu et al.*, 2000; *Peters and Bokhorst*, 2000; and *Burgett et al.*, 2001]. The complex time and spatial variability of most wind-driven shelf flows, however, makes meaningful comparisons of direct turbulence measurements and turbulence submodels in that case an extremely challenging task that requires further research. While efforts along those lines are proceeding, it is sensible to examine the comparative performance of the most widely used turbulence parameterization schemes in relevant shelf circulation problems in order to learn more about the implication of each scheme for the energetic mesoscale flow and for the turbulence variables.

[5] In the present study we continue the two-dimensional modeling effort and focus on the impact of particular turbulent-closure schemes on the mesoscale circulation and on the dynamics of mixing in upwelling and downwelling fronts. The utilization of the two-dimensional approximation provides a useful simplification while still retaining important mixing effects and constitutes a desirable prerequisite to studies involving more complex three-dimensional flows. The main objectives of this study are to examine the structure and dynamics of vertical mixing over the continental shelf forced by upwelling- and downwelling-favorable winds and to examine the sensitivity of the time-dependent upwelling and downwelling circulation to a given turbulent submodel. For simplicity, the numerical experiments here involve wind forcing only with no surface buoyancy flux. In the following we use three popular turbulent submodels, the Mellor-Yamada level 2.5 closure [*Mellor and Yamada*, 1982] (hereinafter MY), the k-ε closure [*Rodi*, 1987] (hereinafter k-ε) and the K-Profile Parameterization [*Large et al.*, 1994] (hereinafter KPP). The mesoscale model and the turbulent closure schemes are described in section 2 and Appendix A, respectively. A description of the numerical experiments is given in section 3. Sections 4 and 5 discuss, respectively, upwelling and downwelling circulation in response to constant wind forcing. A summary and conclusions are presented in section 6.

2. Model Formulation

[6] The Princeton Ocean Model (POM) [*Blumberg and Mellor*, 1987] is based on the hydrostatic primitive equations in sigma coordinates. We use potential density as a variable so that for two dimensional flow the equations are

$$\frac{\partial \eta}{\partial t}+\frac{\partial (uD)}{\partial x}+\frac{\partial \omega}{\partial \sigma}=0, \tag{1}$$

$$\frac{\partial (uD)}{\partial t}+\frac{\partial (u^2D)}{\partial x}+\frac{\partial (u\omega)}{\partial \sigma}-fvD=-gD\frac{\partial \eta}{\partial x}-\frac{gD^2}{\rho_0}\cdot\int_\sigma^0\left(\frac{\partial \sigma_\theta}{\partial x}-\frac{\sigma}{D}\frac{\partial D}{\partial x}\frac{\partial \sigma_\theta}{\partial \sigma}\right)d\sigma+\frac{\partial}{\partial \sigma}\left[\frac{K_M}{D}\frac{\partial u}{\partial \sigma}\right]+2A_M\frac{\partial}{\partial x}\left(D\frac{\partial u}{\partial x}\right), \tag{2}$$

$$\frac{\partial (vD)}{\partial t}+\frac{\partial (uvD)}{\partial x}+\frac{\partial (v\omega)}{\partial \sigma}+fuD=\frac{\partial}{\partial \sigma}\left[\frac{K_M}{D}\frac{\partial v}{\partial \sigma}\right]+A_M\frac{\partial}{\partial x}\left(D\frac{\partial v}{\partial x}\right), \tag{3}$$

$$\frac{\partial (\sigma_\theta D)}{\partial t}+\frac{\partial (\sigma_\theta uD)}{\partial x}+\frac{\partial (\sigma_\theta \omega)}{\partial \sigma}=\frac{\partial}{\partial \sigma}\left[\frac{K_H}{D}\frac{\partial \sigma_\theta}{\partial \sigma}\right]+A_H\frac{\partial}{\partial x}\left(D\frac{\partial \sigma_\theta}{\partial x}\right)+\frac{\partial I}{\partial \sigma}, \tag{4}$$

where (u, v) are the horizontal velocity components in the (x, y) directions, $H(x)$ is the undisturbed water depth, $\eta(x, t)$ is the free surface elevation, $D = H + \eta$, $\sigma = (z - \eta)/D$, z is the original Cartesian vertical coordinate, t is time, ω is the velocity normal to σ surfaces, σ_θ is the potential density, ρ_0 is the constant reference density, f is the Coriolis parameter, g is the acceleration of gravity, I is a solar radiation forcing term, A_M is a constant horizontal eddy viscosity and A_H ($=A_M$) is a constant horizontal diffusivity. The vertical viscosity K_M and diffusivity K_H are given by

$$K_M=\hat{K}_M+\nu_m \tag{5a}$$

$$K_H=\hat{K}_H+\nu_h, \tag{5b}$$

where ν_m and ν_h are constants and where $\hat{K}_M$ and $\hat{K}_M$ are determined by the turbulent submodel (see Appendix A).

[7] Since we find from the experiments that in general $|\eta_t| \ll |(uD)_x|, |\omega_\sigma|$, where subscripts t, x and σ denote partial differentiation, it is useful to neglect η_t in equation (1) and to calculate an approximate streamfunction for the u and ω velocity components. We assume $(uD)_x + \omega_\sigma \approx 0$, define $\Psi_\sigma = uD$, $\Psi_x = -\omega$, and calculate

$$\Psi(x,\sigma)=-\int_{x_0}^{x}\omega(x',\sigma)dx', \tag{6}$$

where $x = x_0$ is the location of the coast. We will also examine the vertical velocity component w along the z axis,

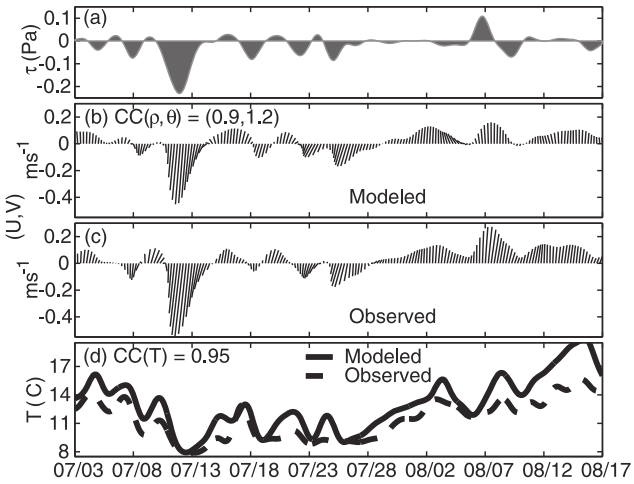

Figure 1. Time series of (a) alongshore wind stress τ, (b) modeled and (c) observed depth-average current vectors (U, V), and (d) model and observed near-surface temperature T, from a mooring in 50 m water depth off Newport, Oregon, during 1999. Adapted from the results presented and analyzed by *Oke et al.* [2002a, 2002b]. CC(ρ, θ) is the amplitude and phase of the complex cross-correlation coefficient between modeled and observed current vectors, and CC(T) is the cross-correlation between the modeled and observed temperatures.

where w is calculated consistently using (u, v, ω) and the definition of ω [*Blumberg and Mellor*, 1987].

[8] The model domain is an across-shelf section (Figure 2) bounded by vertical walls. A right-handed coordinate system is used where x is positive onshore, y is positive northward, and σ varies from $\sigma = 0$ at the surface [$z = \eta(x, t)$] to $\sigma = -1$ at the bottom [$z = -H(x)$]. The offshore boundary is at $x = 0$ and the coast is at $x = x_0$. As in Figure 2, the horizontal distance shown in subsequent figures will be the distance offshore, $x_0 - x$.

[9] The boundary conditions at the surface are

$$\omega = 0 \quad \text{at} \quad \sigma = 0, \tag{7a}$$

$$(K_M/D)(u_\sigma, v_\sigma) = \left(\tau^{(x)}, \tau^{(y)}\right)/\rho_0, \tag{7b}$$

$$(K_H/D)\sigma_{\theta\sigma} = I_1, \quad \sigma \to 0, \tag{7c}$$

where $\tau^{(x)}$ and $\tau^{(y)}$ are the (x, y) components of the surface wind stress, and I_1 is the surface buoyancy flux. In this study we assume no surface buoyancy flux and specify $I_1 = 0$ and likewise in equation (4) $I_\sigma = 0$.

[10] The boundary conditions at the bottom are

$$\omega = 0 \quad \text{at} \quad \sigma = -1, \tag{8a}$$

$$(K_M/D)(u_\sigma, v_\sigma) = \left(\tau_b^{(x)}, \tau_b^{(y)}\right)/\rho_0, \tag{8b}$$

$$(K_H/D)\sigma_{\theta\sigma} = 0, \sigma \to -1, \tag{8c}$$

where the bottom stress components are

$$\left(\tau_b^{(x)}, \tau_b^{(y)}\right) = \rho_0 C_D \left(u_b^2 + v_b^2\right)^{1/2} (u_b, v_b). \tag{9}$$

The bottom velocity components (u_b, v_b) are evaluated at the grid point next to the bottom; that is, at $\sigma_b = -1 + \Delta\sigma_b/2$, where $\Delta\sigma_b$ is the σ finite-difference grid interval at the bottom. The drag coefficient,

$$C_D = \max\left[\kappa^2\{\ln(\Delta z_b/z_{ob} + 1)\}^{-2},\ 2.5 \times 10^{-3}\right], \tag{10}$$

where $\kappa = 0.4$ is the von Kármán constant, z_{0b} is bottom roughness length and $\Delta z_b = \Delta\sigma_b H/2$. The boundary conditions along the vertical sidewalls at the coast ($x = x_0$) and offshore ($x = 0$) are

$$u = 0, \quad v_x = 0, \quad \text{and} \quad \sigma_{\theta x} = 0, \quad \text{at} \quad x = 0, x_0. \tag{11}$$

[11] Three turbulent-closure schemes, MY [*Mellor and Yamada*, 1982; *Galperin et al.*, 1988; *Kantha and Clayson*, 1994], k-ε [*Rodi*, 1987; *Burchard et al.*, 1998] and KPP [*Large et al.*, 1994] are used to compute vertical turbulent fluxes in the mesoscale model. The details of the turbulent schemes are included in Appendix A.

3. Description of Numerical Experiments

[12] The numerical experiments involve initial-value problems for flows forced by essentially constant upwelling- and downwelling-favorable winds similar to those of *Allen et al.* [1995] and *Allen and Newberger* [1996], respectively. Designations for the experiments are based on the turbulent submodel and, in the case of MY and k-ε, on the particular stability functions utilized and are listed in Table 1. Three primary experiments are conducted for each wind condition to study the dependence of the response on

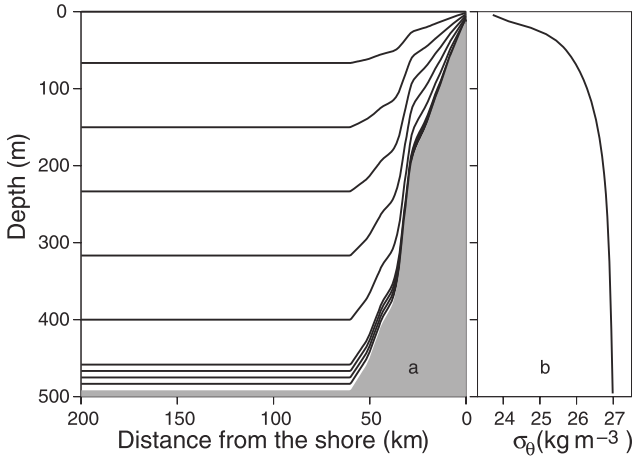

Figure 2. (a) Model computational domain. The shaded area shows the Oregon shelf and slope topography at 41°15′N. The grid spacing is uniform in σ and in x with 60 σ levels; horizontal grid resolution in x is 250 m. The full σ resolution is shown only near the bottom. (b) Initial density field.

Table 1. Summary of Experiments

Model	Turbulence Equations	Stability Function Coefficients (Equation (A12))	limit on l (Equation (A10))	q^2l Production Coefficients (Equation (A2))
MYK	q^2, q^2l	Kantha-Clayson	yes	$E_1 = E_3 = 1.8$
k-εK	$k = q^2/2$, ε	Kantha-Clayson	yes	
KPP				
MYG	q^2, q^2l	Galperin et al.	yes	$E_1 = E_3 = 1.8$
k-εG	$k = q^2/2$, ε	Galperin et al.	yes	
MYO	q^2, q^2l	Galperin et al.	no	$E_1 = E_3 = 1.8$
MYE	q^2, q^2l	Kantha-Clayson	yes	$E_1 = 1.8$, $E_3 = 5.093$

the turbulent mixing scheme, MYK, k-εK or KPP, while keeping topography, stratification, and wind stress forcing unchanged. Four secondary experiments are included for comparison. The first two, denoted by MYG and k-εG, are carried out using the *Galperin et al.* [1988] stability functions, $C_2 = C_3 = 0$ in equation (A12). The third, MYO, uses the *Galperin et al.* [1988] stability functions and replaces equation (A10) by $\hat{l} = l$ as in the original POM. Finally, an experiment, MYE, with $E_3 = 5.093$ in equation (A2) is included based on the recent discussion by *Burchard* [2001].

[13] The initial state corresponds to a stratified coastal ocean at rest with a horizontally uniform density field. The initial conditions are

$$u = v = \omega = 0, \quad \sigma_\theta = \sigma_{\theta 0}(z), \quad q^2 = q^2 l = \varepsilon = \epsilon_0, \quad \text{at} \quad t = 0. \tag{12}$$

where ϵ_0 is a small number taken to be 1×10^{-8}. The wind forcing is a spatially independent alongshore wind stress given by

$$\tau^{(y)} = \tau_0 \sin(t\pi/2T_R), \quad 0 \le t \le T_R \tag{13a}$$

$$\tau^{(y)} = \tau_0, \quad T_R \le t, \tag{13b}$$

where $|\tau_0| = 0.05$ N m^{-2} and $T_R = 2$ days. The constant $\tau_0 < 0$ for upwelling-favorable and $\tau_0 > 0$ for downwelling-favorable winds. The other forcing terms in equations (4), (7b), and (7c) are zero; that is, $\tau^{(x)} = I = I_1 = 0$. As a result, in the KPP scheme $\phi(\varsigma) = 1$, $w_\phi = \kappa\, u_*$, and $\gamma_\phi = 0$.

[14] For all experiments, the topography of the continental shelf and upper slope (Figure 2a) corresponds to that off Oregon at 45°15′N. The initial density $\sigma_{\theta 0}(z)$ (Figure 2b) is obtained by horizontally averaging an observed density field from 29 June 1973. For all experiments, $f = 1.0362 \times 10^{-4}$ s^{-1}. The model domain extends 200 km offshore. The depth at the coast is 10 m and the depth offshore is 500 m. For finite difference solutions, uniform grid spacing in σ is used with 60 σ intervals. As a result, the vertical grid spacing varies from 0.17 m at the coast to 8.33 m in the deepest water. The horizontal grid size is 0.25 km.

[15] The horizontal eddy viscosity and diffusivity are set to be small; that is, $A_M = A_H = 4$ m^2 s^{-1} so that horizontal diffusion processes play a negligible role. We choose $\nu_m = \nu_{m0} = \nu_h = 2 \times 10^{-5}$ m^2 s^{-1}. The roughness parameter $z_0 = 0.01$ m for both surface and bottom boundary layers. The reference density $\rho_0 = 10^3$ kg m^{-3}. Finite difference time steps are 60 s for the baroclinic and 2.5 s for the barotropic components.

4. Upwelling Simulation: Constant Wind Forcing

[16] The model response to an upwelling-favorable wind stress as a function of the turbulent closure scheme is discussed below. We focus on a description of the flow field over the continental shelf with emphasis on turbulent mixing processes. All the variables that are presented have been averaged over an inertial period (hereinafter IP) to isolate subinertial features of the circulation.

4.1. Mesoscale Variability

[17] The across-shelf and depth (x, z) fields of potential density σ_θ, alongshore velocity v, stream function Ψ, vertical velocity w, potential vorticity Π, eddy viscosity $\hat{K}_M$, and eddy diffusivity $\hat{K}_H$ over the shelf at time $t = 24$ IP are plotted in Figure 3. The structures of these fields at 24 IP are qualitatively similar for the three mixing schemes. The figures show the isopycnals upwelled near the coast and the presence of a southward coastal jet in the alongshore velocity v. The across-shelf circulation pattern shown by the stream function Ψ indicates offshore Ekman transport in the surface boundary layer, with onshore transport concentrated in the bottom boundary layer. As shown by Ψ, the offshore flow in the surface layer exhibits a small dip downward on the inner shelf as upwelled water is forced to flow offshore. The offshore flow downwells or subducts on the shoreward side of the dip and upwells on the offshore side. A small-scale recirculation cell is present, and the offshore flow tends to reverse closer to the surface. The potential vorticity, which is defined for a two-dimensional hydrostatic flow in Cartesian coordinates as [*Allen and Newberger*, 1996]

$$\Pi = (f + v_x)\sigma_{\theta z} - v_z\sigma_{\theta x}, \tag{14}$$

is negative everywhere at $t = 0$, and becomes positive in the surface boundary layer for $t > 0$. Large values of $\Pi > 0$ are associated with the dip, indicating that spatial fluctuations in the offshore flow may be due to slant-wise convection resulting from hydrostatic symmetric instability. The sign change of Π is a necessary condition for a generation of inviscid symmetric instability in the surface layer flow [e.g., *Allen and Newberger*, 1998].

[18] Differences in the turbulent closure schemes can be seen in the fields of $\hat{K}_H$ and $\hat{K}_M$. Although the depth of the surface mixing layer is similar for all three schemes, the structure within this layer depends upon the submodel. The region with $\hat{K}_M$ and $\hat{K}_H$ near 0.01 is nearly uniform

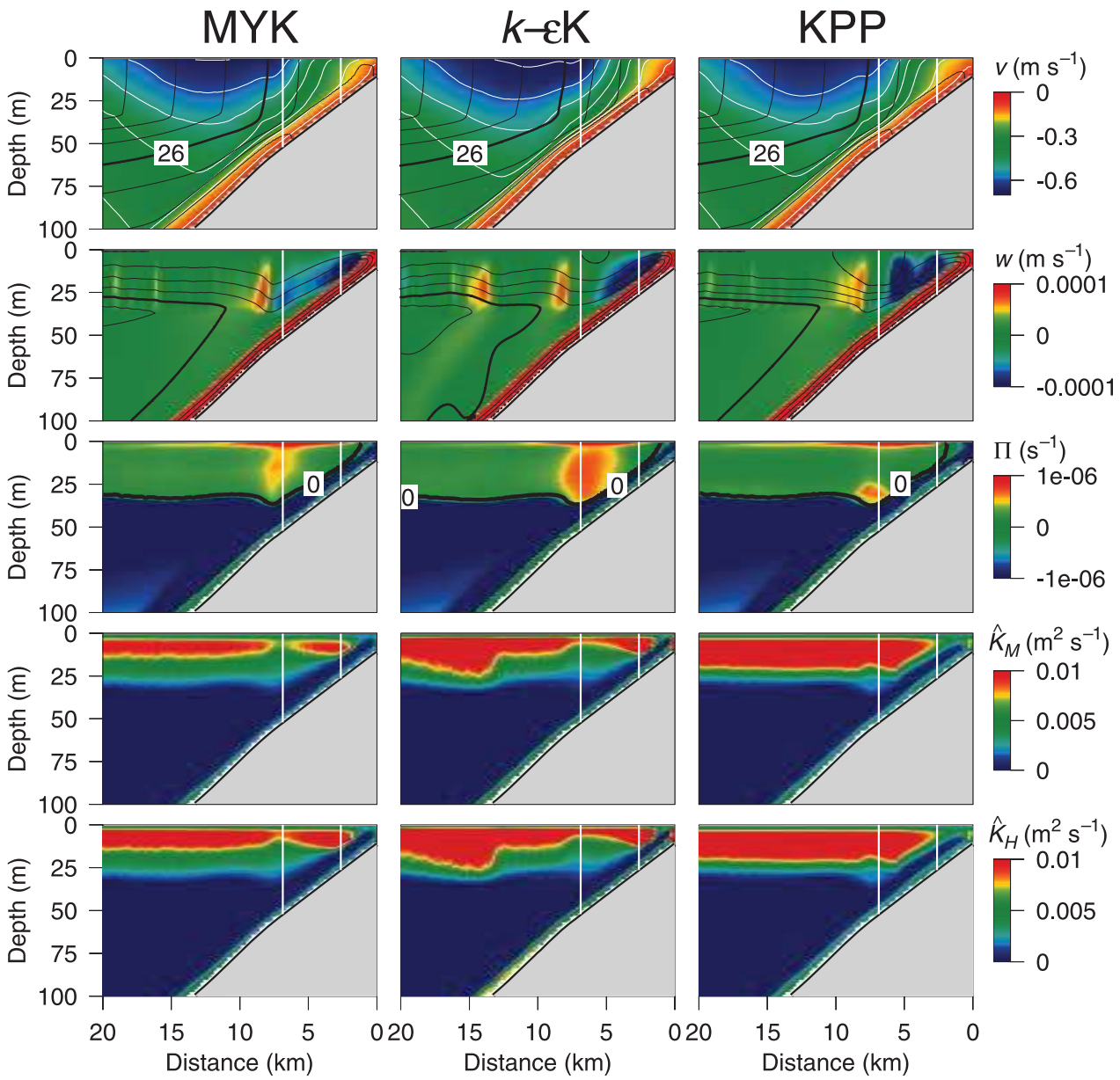

Figure 3. Fields of alongshore velocity v (color contours and white contour lines) together with density σ_θ (black contour lines), vertical velocity w (color contours) together with the stream function for the across-shelf flow Ψ (black contour lines), potential vorticity Π, eddy viscosity $\hat{K}_M$ and eddy diffusivity $\hat{K}_H$ for the MYK, k-εK and KPP mixing schemes at t = 24 IP (≈day 17). All variables are averaged over an inertial period. The contour intervals are $\Delta\sigma_\theta = 0.2$ kg m^{-3}, where $\sigma_\theta = 26$ kg m^{-3} is marked by a heavy line; $\Delta v = 0.1$ m s^{-1}; $\Delta\Psi = 0.1$ m^2 s^{-1}, where $\Psi = 0.4$ m^2 s^{-1} is marked with a heavy line. The vertical white lines mark the locations of profiles to be discussed in detail.

offshore for KPP and extends to about 20 m. The vertical structure for KPP depends primarily on the shape function G which does not vary much across-shelf offshore of the velocity front since the surface friction velocity is constant and the depth of the well mixed layer is nearly constant. For MYK, the region of relatively large $\hat{K}_H$ and $\hat{K}_M$ is shallower (about 15 m) and has a pronounced minimum at the location of the dip in Ψ. There is considerable additional across-shelf variation in the magnitude of $\hat{K}_H$ and $\hat{K}_M$ for k-εK with a small vertical extent at the dip and a sharp increase in thickness about 15 km offshore.

[19] The time evolution of vertical profiles of u, v, σ_θ, $\hat{K}_M$, and $\hat{K}_H$ at the 52-m isobath, 6.9 km offshore, and at the 26-m isobath, 2.6 km offshore, is shown in Figures 4 and 5. The locations of these profiles are shown as vertical white lines in Figure 3 with the offshore profile at the maximum of the potential vorticity Π and the second profile inshore of the coastal jet. Results from the three models show considerable agreement. In particular, the surface and bottom layer thicknesses are nearly identical for the three models (Figures 3, 4, and 5) and the velocity and density magnitudes and shapes are similar. In general, $\hat{K}_M$ and $\hat{K}_H$ have

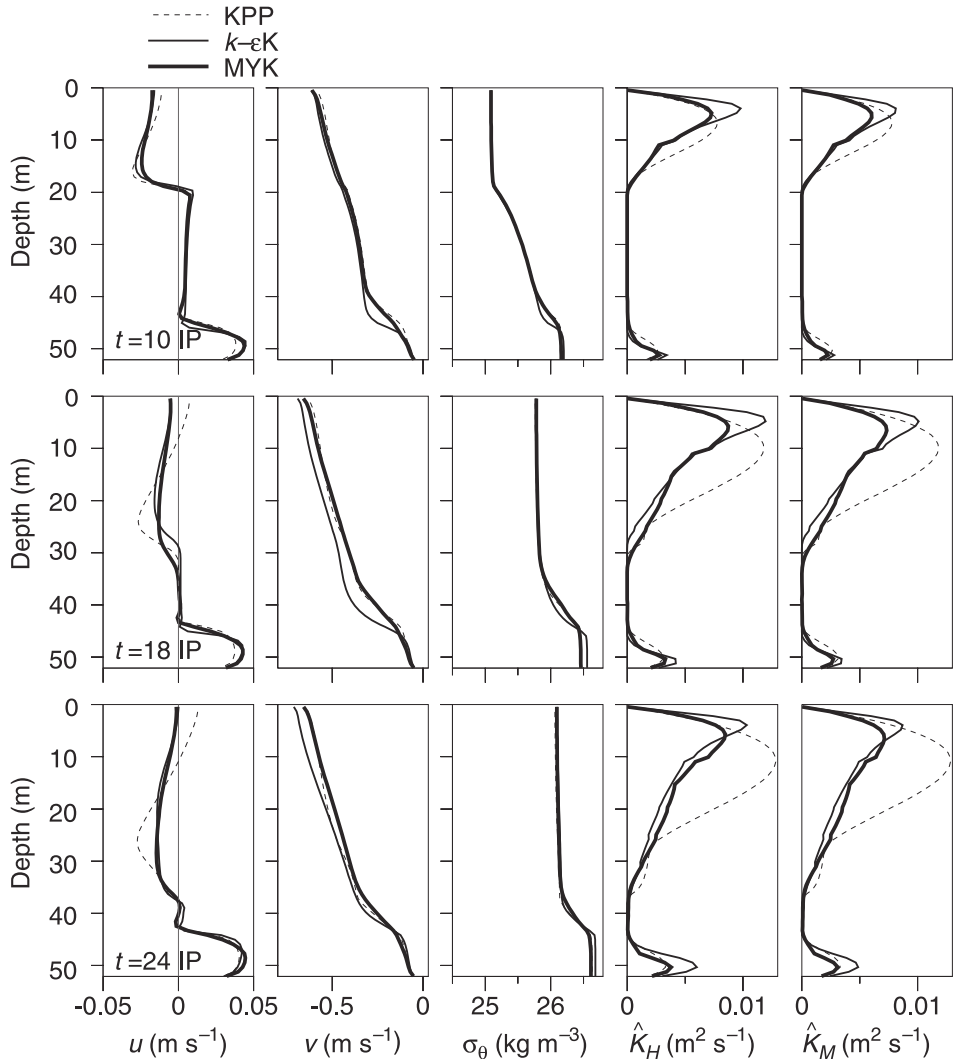

Figure 4. Vertical profiles at the 52-m isobath (6.9 km offshore) of u, v, σ_θ, $\hat{K}_H$ and $\hat{K}_M$ for t = 10 IP (≈day 7), 18 IP (≈day 15) and 24 IP (≈day 17). The dashed, thin and thick lines denote, respectively, the KPP, k-εK and MYK submodels. The thin shaded line is u = 0 m s^{-1}.

local maxima in the surface and the bottom boundary layers with small values in the stratified interior.

[20] The 52-m isobath is located within the alongshore jet at all times shown. At t = 10 IP the surface and bottom mixed layers are separated by a large inviscid region with small onshore velocities, large density gradients and very small values of $\hat{K}_M$ and $\hat{K}_H$. By t = 18 IP the surface layer had deepened significantly and by t = 24 IP there is only a 10-m stratified, inviscid region between the surface and bottom layer. The near-surface peaks in $\hat{K}_H$ and $\hat{K}_M$ are sharpest for k-ε and broadest with a deep maximum for KPP, consistent with the pattern seen in Figure 3. The shape of $\hat{K}_M$ and $\hat{K}_H$ for KPP depends primarily on the cubic equation for the shape function G and is fit smoothly to the values in the interior region so that there is little structure within the boundary layers. A region of increased $\hat{K}_M$ and $\hat{K}_H$ due to the Richardson number parameterization in the interior can be seen at the bottom of the surface layer for KPP at t = 24 IP. The vertical gradient of the across-shore velocity u in the surface layer is greatest for KPP with onshore flow near the surface at t = 18 IP and t = 24 IP reflecting the recirculation cell above the dip shown in the streamfunction Ψ field in Figure 3.

[21] The 26-m isobath is within the alongshore jet at t = 10 IP, and the profiles exhibit the features seen at the 56-m isobath at later times. At t = 18 and 24 IP this location is inshore of the jet and the alongshore velocities are smaller. The potential density is approximately constant in both the surface and bottom layer with a sharp gradient in the small region between. There is nearly uniform offshore flow in a surface layer and onshore flow in a bottom layer. The coefficients $\hat{K}_M$ and $\hat{K}_H$ are large in the surface layer, especially for k-ε at t = 24 IP (≈0.2 m^2 s^{-1}).

[22] The KPP scheme computes $\hat{K}_M$ and $\hat{K}_H$ as a product of boundary layer height, velocity scale, and nondimensional shape function $G(\xi)$ in boundary layers (equation (A28)), and as a function of gradient Richardson number in the stratified interior (equation (A36)). For constant wind-driven simulations, the vertical structure of $\hat{K}_M$ and $\hat{K}_H$ in the boundary layers is determined primarily by $G(\xi)$,

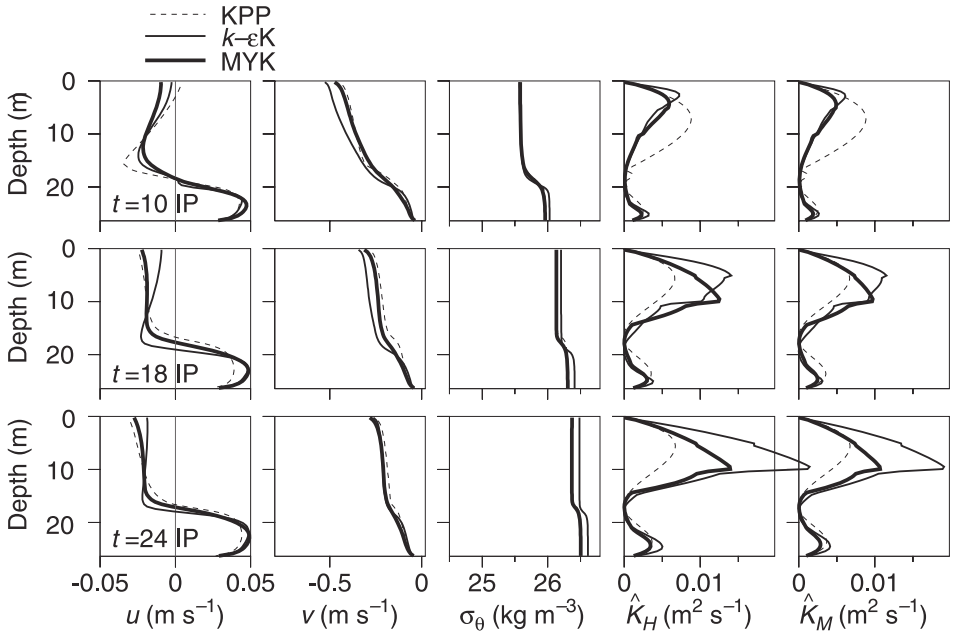

Figure 5. Vertical profiles at the 26-m isobath (2.6 km offshore) of u, v, σ_θ, $\hat{K}_H$ and $\hat{K}_M$ as in Figure 3.

because the turbulent velocity scale is independent of depth and the nonlocal transport term γ_ϕ is zero. The turbulent velocity scale is proportional to the friction velocity, equation (A15) or (A17), and the height of the boundary layer is determined from the bulk Richardson number criterion. The properties of G are determined from similarity scaling and boundary matching conditions at the stratified interface. Although KPP diffusivities are similar to MYK and k-εK, there is no obvious physical explanation for why a cubic polynomial provides a best fit for eddy diffusivity and viscosity in boundary layers.

4.2. Small-Scale Variability: Comparison of MY and k-ε

[23] The MY and k-ε closure schemes have the advantage that they produce fields of the turbulence quantities. The KPP model does not and thus cannot be included in this comparison. Both MY and k-ε schemes compute $\hat{K}_M$ and $\hat{K}_H$ as a product of a velocity scale, a turbulent length scale, and nondimensional stability functions. We expect similarities between MYK and k-εK outputs simply because both are local two equation closure schemes and use identical forms of the *TKE* ($q^2/2$) equation (A1) and the same stability functions (equation (A12)). The major difference between MY and k-ε is the way in which the turbulent length scale is computed. Fields of *TKE*, computed length scale l, effective length scale $\hat{l}$ (equation (A10)) used to compute the eddy diffusivity and eddy viscosity (equation (A9)), and the stability functions S_M and S_H (equation (A12)) are shown at t = 24 IP in Figure 6. The most noticeable difference between these models is found in the length scale l. This will be analyzed below. The fields of *TKE*, $\hat{l}$, S_H and S_M which are used in the calculation of $\hat{K}_H$ and $\hat{K}_M$ (equation (A9)) are qualitatively similar for the two schemes with the TKE produced by the k-ε scheme somewhat larger. The largest values of *TKE* are found in the surface layer and are located near the dip in the stream function Ψ (Figures 3 and 4). The majority of turbulent mixing over the shelf occurs in the regions where either the across-shelf or along-shelf transport is large. These regions include the surface and bottom boundary layers and the part of the southward flowing coastal jet where density stratification is weak and the vertical shear of the mesoscale currents is large. There are maxima in the stability functions S_H and S_M located inshore of the jet consistent with the large $\hat{K}_M$ and $\hat{K}_H$ at the 26-m isobath shown in Figure 5.

[24] Fields of terms from the *TKE*equation (A1), including shear production P (equation (A3a)), buoyancy production B (equation (A4a)), dissipation rate ε (equation (A5a)), and the vertical diffusion of turbulent kinetic energy D_V (equation (A6a)) at t = 24 IP are shown in Figure 7 for the MYK and k-εK experiments. Note that the definition of the zplotted terms is such that ε is approximately equal to the sum of the other terms. The time variability and advection terms (not shown) are small. As shown in Figures 6 and 7, the mixing structure in the coastal jet is horizontally asymmetric about the jet axis which is located about 12 km offshore at t = 24 IP (Figure 3). The coastal jet has the strongest vertical shear on the shoreward side, where *TKE*, shear production, dissipation and buoyancy flux are all large (Figures 3, 6, and 7). In the inshore region of large S_M and S_H shown in Figure 6, the buoyancy flux B is positive indicating that the surface layer is weakly unstably stratified leading to the large values of $\hat{K}_H$ and $\hat{K}_M$ shown in Figure 5.

[25] The nature of mixing on the inner part of the shelf is different from that in the coastal jet and in the midshelf boundary layers. The positive buoyancy flux on the inner shelf is a signature of convective overturning (Figure 7). Here, potential energy is converted to *TKE*, and buoyancy production is a source for *TKE*. In shear-driven mixing such as occurs in the coastal jet, buoyancy flux is negative and opposes shear production. It appears that the upwelled water on the inner shelf becomes gravitationally unstable as wind stress forces the surface-layer flow offshore.

[26] To look more closely at the mixing near the maximum of *TKE* and potential vorticity Π (Figures 3 and 7),

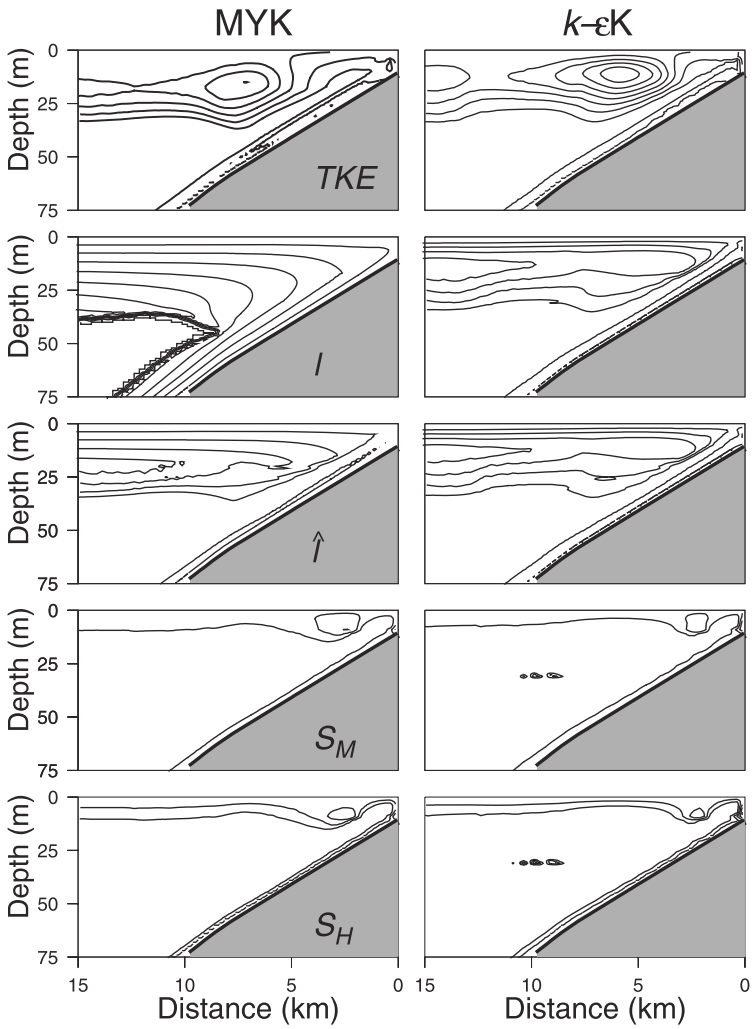

Figure 6. Fields of turbulent quantities at t = 24 IP for (left) MYK and (right) k-εK. Variables include $TKE = \frac{1}{2}q^2$ (J kg^{-1}), turbulent length scale l (m), effective length scale $\hat{l}$ (m) (equation (A10)) used to calculate $\hat{K}_M$ and $\hat{K}_H$, the stability function of eddy viscosity S_M and the stability function of eddy diffusivity S_H. Contour intervals are $\Delta TKE = 1 \times 10^{-4}$, $\Delta l = \Delta\hat{l} = 1$, $\Delta S_H = \Delta S_M = 0.2$.

we examine the terms in the turbulence equations for MYK and k-εK. Vertical profiles of terms in the *TKE* equations at the 52-m isobath for t = 24 IP are shown in Figures 8a and 8b. Note that the advection and time variability of *TKE* are significantly smaller than the other terms and are not shown. For both MYK and k-εK schemes a production P and dissipation ε balance holds near the surface and the bottom, and a production P, dissipation ε, and buoyancy B balance holds for the rest of the water column. Local peaks in P, ε, and B near the top of the bottom boundary layer characterize entrainment mixing, which is stronger in the k-εK scheme than in the MYK scheme (Figure 8). Nearly 10% of the shear-production P is balanced by negative buoyancy production B in regions where the P, ε, and B balance holds. Vertical profiles of the terms in the q^2l and ε equations are plotted in Figures 8c and 8d. In general, production and dissipation are the largest terms in both the q^2l and ε budgets. The advection and time derivative terms are small and are not plotted. As shown in Figure 8c, $P_l + B_l - \varepsilon_l \approx 0$ for most of the water column, except near the surface and the bottom boundaries, where D_{Vl} also contributes to the q^2l budget. The dissipation term ε_l in the q^2l equation has two components: a local sink ε (marked with crosses in Figure 8c) and a nonlocal sink $\varepsilon\ E_2(l/\kappa L)^2$. Both components are important in determining ε_l. In the ε budget, the dissipation term ε is larger than the production term P_ε (Figure 8d), near the top and bottom boundaries where $\varepsilon \approx P_\varepsilon + D_{V\varepsilon}$. The buoyancy term B_ε (equation (A20b)) is positive throughout the water column and acts as a source to the ε budget independent of the stability, whereas B_l (equation (A3b)) is negative for stable stratification; that is, it acts as a sink of q^2l.

[27] Vertical profiles of *TKE* ($q^2/2$), l, $\hat{l}$, S_M, $\hat{K}_H$, $\hat{K}_M$ and ε at the 52-m isobath at t = 24 IP are shown in Figure 9. The top row shows the profiles for the MYK and k-εK experiments using the parameters from *Kantha and Clayson* [1994], the middle row repeats MYK and includes both MYG and k-εG that utilize the parameters of *Galperin et al.* [1988], the bottom row repeats MYK and includes MYE with E_3 = 5.093 in equation (A2) ([*Burchard*, 2001] and

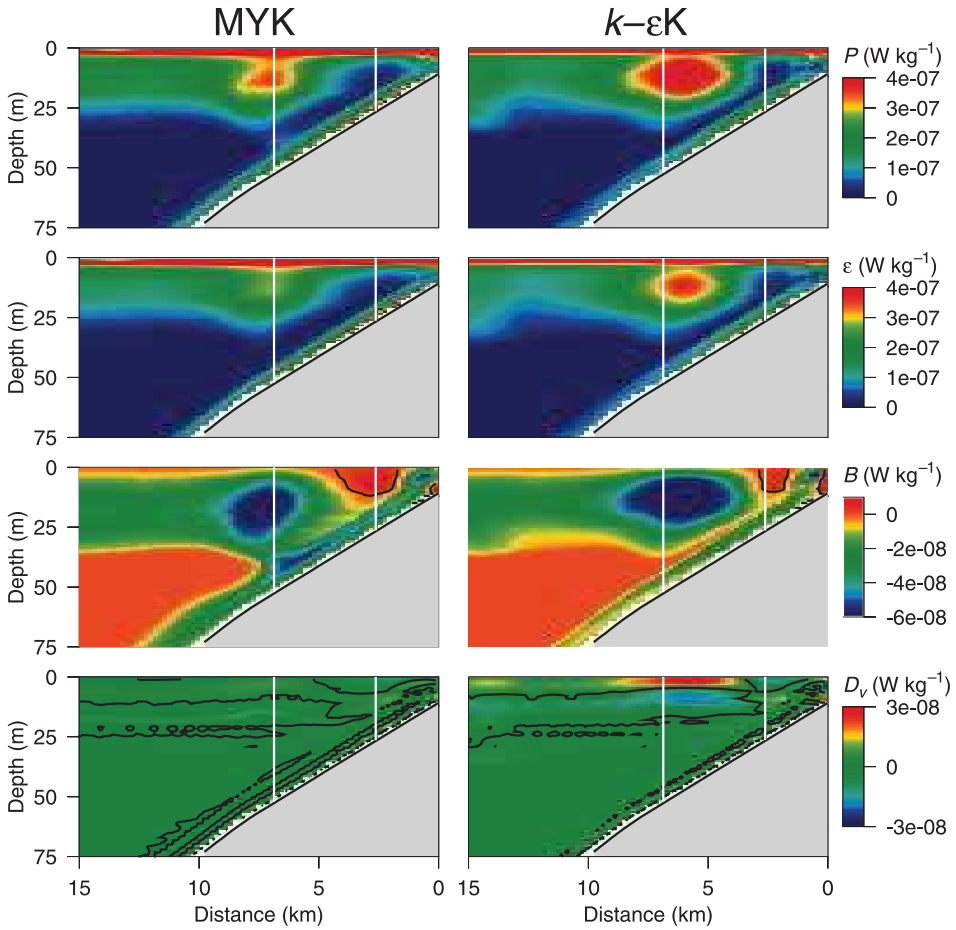

Figure 7. Fields on the inner shelf of terms from the turbulent kinetic energy equation (A1) for (left) MYK and (right) k-εK at t = 24 IP (≈ day 17): shear production P (equation (A3a)), dissipation rate ε (equation (A5a)), buoyancy production B (equation (A4a)) and vertical diffusion D_V (equation (A6a)). The thick solid lines in the D_V and B plots denote the $D_V = 0$ and $B = 0$ contours. The vertical white lines mark the locations of profiles discussed in detail in the text.

Appendix B) and MYO with the *Galperin et al.* [1988] parameters and $\hat{l} = l$ as in the original POM (Table 1 and Appendix A). S_H and S_M are functions of $G_H = -\hat{l}^2N^2/q^2$ and increase as G_H increases (becomes less negative). Therefore, S_H and S_M are large for weak or unstable stratification and for large values of *TKE*. Since $\hat{l} \leq 0.53\ q/N$ (equation (A10)), G_H is required to be greater than or equal to -0.272 and $G_H = -(0.53)^2 = -0.272$ when $\hat{l} = 0.53\ q/N$. Thus, S_H and S_M take on their minimum values whenever $\hat{l} < l$. Note that large values of $\hat{K}_H$ and $\hat{K}_M$ can exist even in regions where this limit is in effect. For example, in k-εK near the bottom of the surface layer (at approximately −12 m) where larger q^2 and $\hat{l}$ for k-εK and larger S_M and S_H for MYK result in similar values of $\hat{K}_H$ and $\hat{K}_M$ (Figure 9). For all of the models, large dissipation rates ε are found in the surface and bottom layers with substantial dissipation occurring throughout the region where the *TKE* levels are significant.

[28] From Figure 9 we see that MYK and MYG are almost indistinguishable. In both, there is a large difference between l and $\hat{l}$ in the stably stratified, low mixing region above the bottom boundary layer. In contrast, l and $\hat{l}$ agree closely for k-εK and for MYE. There is more difference between k-εK and k-εG than between MYK and MYG where for k-εG l and $q^2/2$ are larger in the top 20 m and there is a greater difference between l and $\hat{l}$. We examine the steady state nature of the length scale below and in Appendix B (for $E_3 \neq E_1$) to attempt to understand this behavior. Note that MYO which uses $\hat{l} = l$ from the q^2l equation in the calculation of the turbulent quantities has small values of $\hat{K}_H$ and $\hat{K}_M$ in the stratified interior despite the fact that l is greater that the $0.53qN^{-1}$ limit in this region. The stability functions S_H and S_M can approach zero without the limit on $\hat{l}$ (equation (A10)). We see that different combinations of the stability functions, the turbulent velocity scale q and turbulent length scale $\hat{l}$ can result in similar values of $\hat{K}_H$ and $\hat{K}_M$.

[29] To illustrate further the effects on the mesoscale flow of changing the turbulence scheme, we consider the near-surface alongshore velocity at t = 24 IP. Across-shelf profiles are shown for k-εK, MYK, MYE, MYO and, for comparison, KPP (Figure 10). The location of the jet agrees well for the four schemes with KPP having the smallest magnitude and MYO the largest. Although the turbulence quantities differ, the near-surface expression of the alongshore upwelling jet is quite similar.

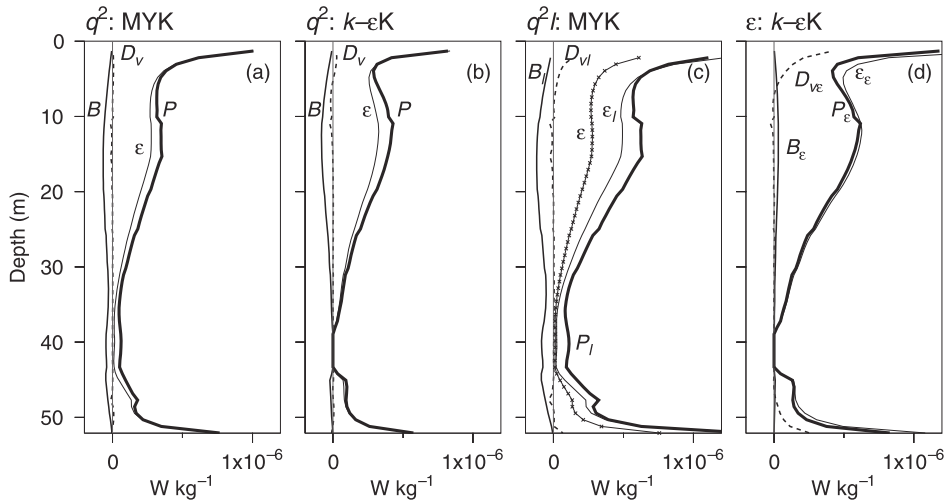

Figure 8. Vertical profiles at the 52-m isobath (6.9 km offshore) at t = 24 IP of the terms in the *TKE* equation (A1) for (a) MYK and (b) k-εK. Shown are shear production P (thick solid line), buoyancy production B (medium solid line), dissipation rate ε (thin solid line) and vertical diffusion D_V (dashed line). (c) Terms in the q^2l equation (A2) of MYK, with ε shown with crosses, and (d) the ε equation (A19) of k-εK. Other lines are as for the corresponding terms in Figures 8a and 8b. The zero line is shaded. Note that all of the terms plotted, defined in equations (A3a)–(A6), (A20) and (A21), have units of dissipation ε (W kg^{-1}); that is, the terms in equations (A1), (A2), and (A19) are divided by $2D$, Dl, and D ($2\varepsilon/q^2$), respectively.

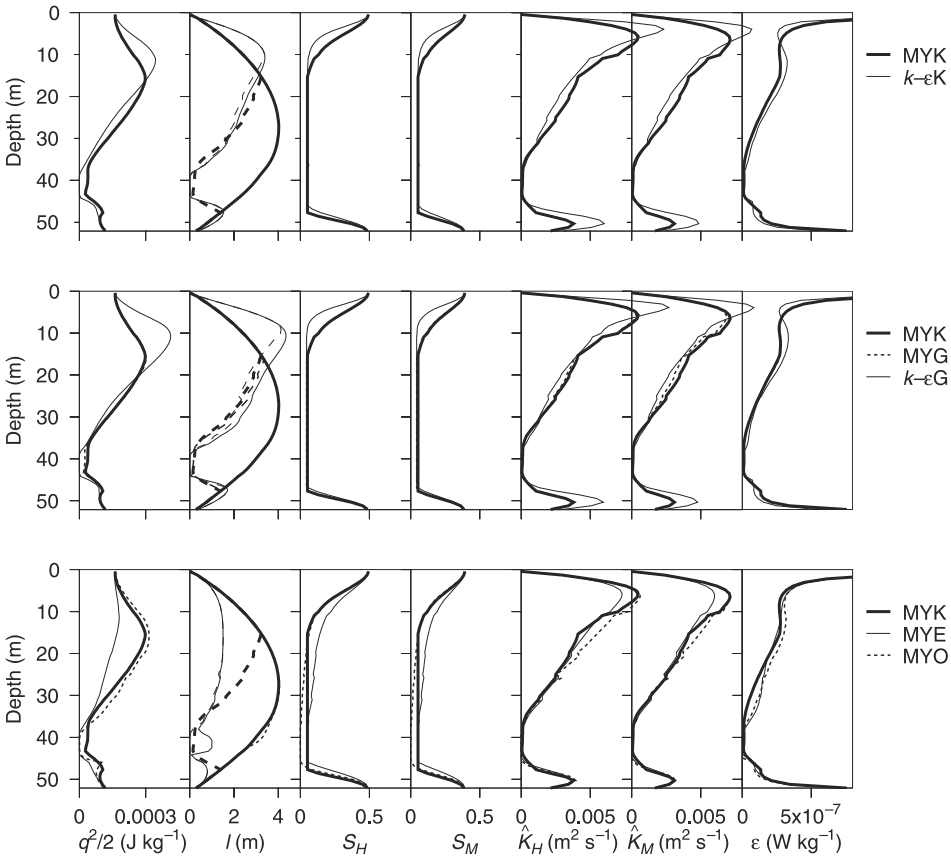

Figure 9. Vertical profiles at the 52-m isobath of $\frac{1}{2}q^2$, l, $\hat{l}$ (long-dashed line), S_H, S_M, $\hat{K}_H$, $\hat{K}_M$ and ε at t = 24 IP; (top) MYK and k-εK; (middle) MYK, MYG and k-εG; (bottom) MYK, MYE and MYO.

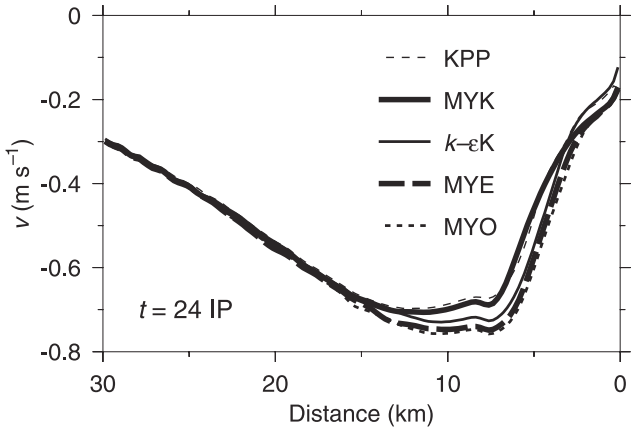

Figure 10. Near-surface alongshore velocities in the upwelling jet at $t = 24$ IP as a function of distance offshore from the MYK, MYE, MYO, k-εK and KPP schemes.

[30] The MYK length scale, $l = (q^2 l/q^2)$ ($\equiv l^{MY}$) increases away from boundaries, and becomes largest at the edge of the boundary layers. The value of l when q^2 or $q^2 l$ are near zero is essentially meaningless and is arbitrarily set to 1 m as in the center of the domain in Figure 6. The k-εK length scale gradually increases away from the boundary, attains a subsurface maximum, and then decreases as stratification increases (Figures 6 and 9). For regions where buoyancy production is important in the *TKE* budget, it is shown below and illustrated in Figures 6 and 9 that the turbulent length scale of k-εK scales similarly to the buoyancy scale $0.53qN^{-1}$. On the other hand, the effective length scale for the MYK scheme is selected by choosing the minimum value between l^{MY} and $0.53qN^{-1}$ where these two quantities can differ appreciably.

[31] To understand the steady state nature of the MY length scale, we examine q^2 and $q^2 l$ equations by neglecting vertical diffusion and advection in equations (A1) and (A2), to obtain

$$P + B - \varepsilon = 0 \tag{15}$$

$$E_1 P + E_3 B - \hat{W}\varepsilon = 0, \tag{16}$$

where $E_1 = E_3 = 1.8$ and $\hat{W}$ is defined in equation (A7). The steady state solution requires $\hat{W} = E_1$, and the corresponding equilibrium length scale becomes,

$$l_{eq}^{MY} = \left(\frac{E_1 - 1}{E_2}\right)^{1/2} \kappa L. \tag{17}$$

For $E_1 = 1.8$, $E_2 = 1.33$, and $\kappa = 0.4$, $l_{eq}^{MY} = 0.3\ L$. Consequently, the equilibrium length scale is proportional to L(A7) and is independent of stratification, shear, Richardson number, or any other dynamical variable, which might represent mixing in stratified fluids. The vertical variation of l^{MY} closely follows that of l_{eq}^{MY} for MYK (Figure 11), and both scales deviate notably from $0.53qN^{-1}$ (Figures 6 and 9). We conclude from Figures 9 and 11 that, with the Mellor-Yamada [*Mellor and Yamada*, 1982] parameter values $E_1 = E_3$, the $q^2 l$ equation does not produce a physically meaningful steady-state length scale when vertical stratification is important.

[32] There is no steady state Richardson number solution to equations (15) and (16) [*Burchard*, 2001]. As a proposed change to MY, *Burchard* [2001] introduces $E_3 \neq E_1$, that is, unequal contributions of P and B in the $q^2 l$ equation (A2), and obtains a steady state solution by neglecting divergence terms and by approximating $\hat{W} = 1$. He argues that physically sound results are obtained by changing the relative contribution of the buoyancy production, that is by changing the value of E_3. However, the appropriate contributions of P, B and ε in the length scale equation are not well established. An analysis, similar to *Burchard* [2001] but applicable here where $\hat{W}$ is given by equation (A7), is included in Appendix B. As seen in Figure 9, l and $\hat{l}$ behave similarly for the choice $E_3 = 5.093$ (see Appendix B) with the other parameters as in the work by *Kantha and Clayson* [1994], but the corresponding values of $\hat{K}_M$ and $\hat{K}_H$ in the surface layer are reduced appreciably.

[33] Unlike the MY $q^2 l$ equation, the ε equation has unequal contributions from P and B, and as a result there exits a unique steady state Richardson number and equilibrium length scale solution. Using a production, dissipation, and buoyancy balance in the $k(q^2/2)$ and ε equations (A1) and (A19) reduce to

$$P + B - \varepsilon = 0 \tag{18}$$

$$c_{\varepsilon 1} P + c_{\varepsilon 3} B - c_{\varepsilon 2}\varepsilon = 0. \tag{19}$$

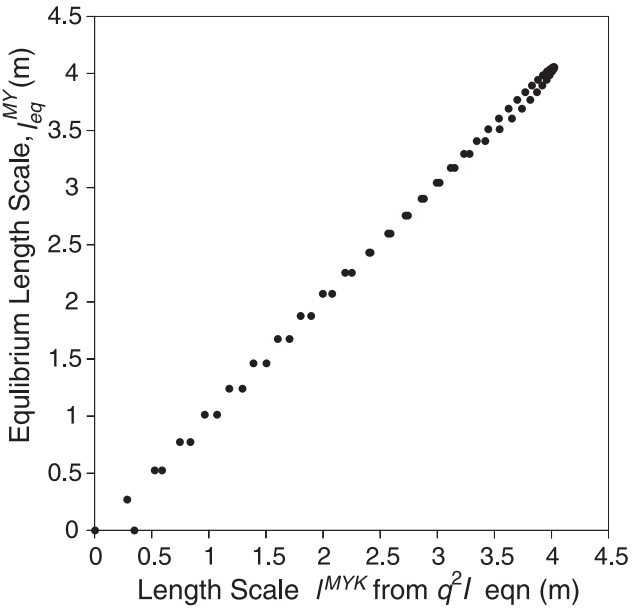

Figure 11. Turbulent length scale l computed from the $q^2 l$ equation (A2) is plotted against the equilibrium length scale computed from equation (17) from experiment MYK. The results are from the vertical profiles at the 52-m isobath at $t = 24$ IP as shown in Figure 8.

A steady flux Richardson number R_f becomes

$$R_f = \frac{-B}{P} = \frac{c_{\varepsilon 2} - c_{\varepsilon 1}}{c_{\varepsilon 2} - c_{\varepsilon 3}}. \quad (20)$$

We find the steady state $R_f \backsimeq 0.2$ for $c_{\varepsilon 1} = 1.44$, $c_{\varepsilon 2} = 1.92$, and $c_{\varepsilon 3} = -0.4$ [*Burchard et al.*, 1998], which is consistent with laboratory measurements [e.g., *Rohr et al.*, 1988], and also with assumptions used in microstructure-based eddy flux estimates [e.g., *Osborn*, 1980].

[34] Substituting $B = -qlS_H N^2$ (equation (A4)), ε (equation (A5)), S_H (equation (A12a)), and $G_H = -l^2 N^2 q^{-2}$ (equation (A13)) in equations (19) and (20), we obtain the following expression for the equilibrium length scale,

$$l_{eq}^{k-\varepsilon} = \frac{q}{N} \cdot \left[\frac{-(c_{\varepsilon 1} - c_{\varepsilon 2})}{(c_{\varepsilon 1} - c_{\varepsilon 2})(3A_2B_2(1 - C_3) + 18A_1A_2) + (c_{\varepsilon 1} - c_{\varepsilon 3})A_2B_1\left(1 - 6A_1B_1^{-1}\right)} \right]^{1/2}. \quad (21)$$

We can rewrite equation (21) using the above values for ($c_{\varepsilon 1}$, $c_{\varepsilon 2}$, $c_{\varepsilon 3}$) and the constants given by *Kantha and Clayson* [1994] as

$$l_{eq}^{k-\varepsilon} = 0.9\frac{q}{N} \equiv 3.48\left(\frac{\varepsilon}{N^3}\right)^{1/2}. \quad (22)$$

For $c_{\varepsilon 3} = -0.534$, we can obtain $l_{eq}^{k\text{-}\varepsilon} = 0.53q/N = 1.5(\varepsilon/N^3)^{1/2}$ and $R_f = 0.195$. We note that with $C_3 = 0$ as in work by *Galperin et al.* [1988] the length scale $l_{eq}^{k\text{-}\varepsilon}$ is imaginary so that an equilibrium length scale is not defined in that case. In fact, $C_3 > 0.145$ is required for $l_{eq}^{k\text{-}\varepsilon}$ to be real. Alternatively, with $C_3 = 0$, $c_{\varepsilon 3} < -0.6$ is required for $l_{eq}^{k\text{-}\varepsilon}$ to be real. Figure 9 shows that the value of l computed for k-εG does not agree as well with $\hat{l}$ as does the value of l from k-εK which has a meaningful equilibrium length scale.

[35] The steady state solution of the k-εK scheme produces a turbulent length scale $l_{eq}^{k\text{-}\varepsilon}$ equation (22) that is proportional to the buoyancy length scale [e.g., *Galperin et al.*, 1988] in the stratified water column. The steady state solution also is consistent with oceanic observations. For example, the last 2 decades of microstructure observations indicate that on average, the physically observable length scale, the Thorpe scale [*Thorpe*, 1977], is approximately equal to the Ozmidov length scale $L_O = (\varepsilon/N^3)^{1/2}$ [*Ozmidov*, 1965; *Dillon*, 1982], whenever vertical stratification is important. A conclusion to be drawn from Figure 9 and equation (22) is that, with the constants in equation (A12) given by *Kantha and Clayson* [1994], the k-ε scheme provides a physically meaningful length scale for both the stratified interior and the top and bottom boundary layers.

5. Downwelling Simulation: Constant Wind Forcing

5.1. Mesoscale Variability

[36] The (x, z) fields of σ_θ, v, Ψ, w, Π, $\hat{K}_M$, and $\hat{K}_H$ at $t = 24$ IP are plotted in Figure 12 for the case of downwelling-favorable wind. A dominant feature of the flow response is a downwelling front at about 8 km from the coast characterized by large, nearly depth independent, horizontal gradients in the alongshore velocity v, large horizontal gradients of density near the bottom at the same location, and by vertically well-mixed density inshore of the front. The velocity front is sharpest in the k-εK model with the MYK and KPP velocity fronts comparable. The near-surface density field shows an evolution of three distinct mixed layer regimes. A surface Ekman layer forms over the midshelf as reported by *Allen and Newberger* [1996], where the mixed layer depth is approximately uniform in the across-shore direction. The mixed layer becomes shallowest at the downwelling front, and then increases abruptly on the shoreward side of the front in a region on the inner shelf where density is vertically mixed throughout the water column. As shown in Figure 12, the density field splits in the vicinity of the downwelling front, where one branch of the density outcrops on the offshore side of the velocity front and the other branch is in the vertically mixed region near the shore. The outcropping isopycnals generate a shallow mixed layer offshore of the downwelling front. The density field supports a coastal jet with a subsurface maximum where turbulent mixing is weak. The inner shelf exhibits a lateral density gradient with vertically-mixed density increasing offshore, a weak alongshore velocity, relatively large values of eddy viscosity and eddy diffusivity and no Ekman layer [e.g., *Allen and Newberger*, 1996]. As shown in the across-shelf stream function, the downwelling front includes a circulation cell extending from surface to bottom. On the shoreward side of the cell, surface water moves down while on the offshore side near-bottom water upwells.

[37] The nature of the offshore flow in the bottom boundary layer is found to vary as wind forcing continues similar to the results of *Allen and Newberger* [1996]. By $t = 24$ IP the flow near the bottom generates temporal and spatial oscillations and recirculation cells (Figure 12). These features have been identified as symmetric instabilities [*Allen and Newberger*, 1996, 1998] based partly on the positive values of potential vorticity Π that are evident in the same region.

[38] The time evolution of vertical profiles of u, v, σ_θ, $\hat{K}_M$, and $\hat{K}_H$, at the 41-m and 63-m isobaths is shown in Figures 13 and 14. These locations are indicated by vertical white lines on Figure 12. The 41-m isobath is on the inner shelf and is in the recirculating cell just offshore of the downwelling front at $t = 10$ IP and in the well mixed region inshore of the front at the later times. At $t = 10$ IP there is strong onshore flow at the surface and offshore flow at middepths. The weak onshore flow at the bottom reflects the beginning of the bottom layer instabilities. The mixing is large only in a surface layer with the layer extending deepest for KPP and shallowest for k-εK. For times $t = 18$ IP and $t = 24$ IP after the front passes this location, the potential density is nearly constant with depth and the surface boundary layer extends to the bottom. For the KPP this implies that the mixing coefficients are determined for the full depth by the nondimensional shape function G (equation (A30)) which results in greater mixing in the interior than in MYK or k-εK. The jagged structure seen in the MYK and k-εK profiles results from small variations in the vertical gradient of the density. The velocities are in good agreement for all three schemes. However, there is small offshore flow at the surface and onshore flow near the bottom for KPP which can be seen in the Ψ field of Figure 12 as well.

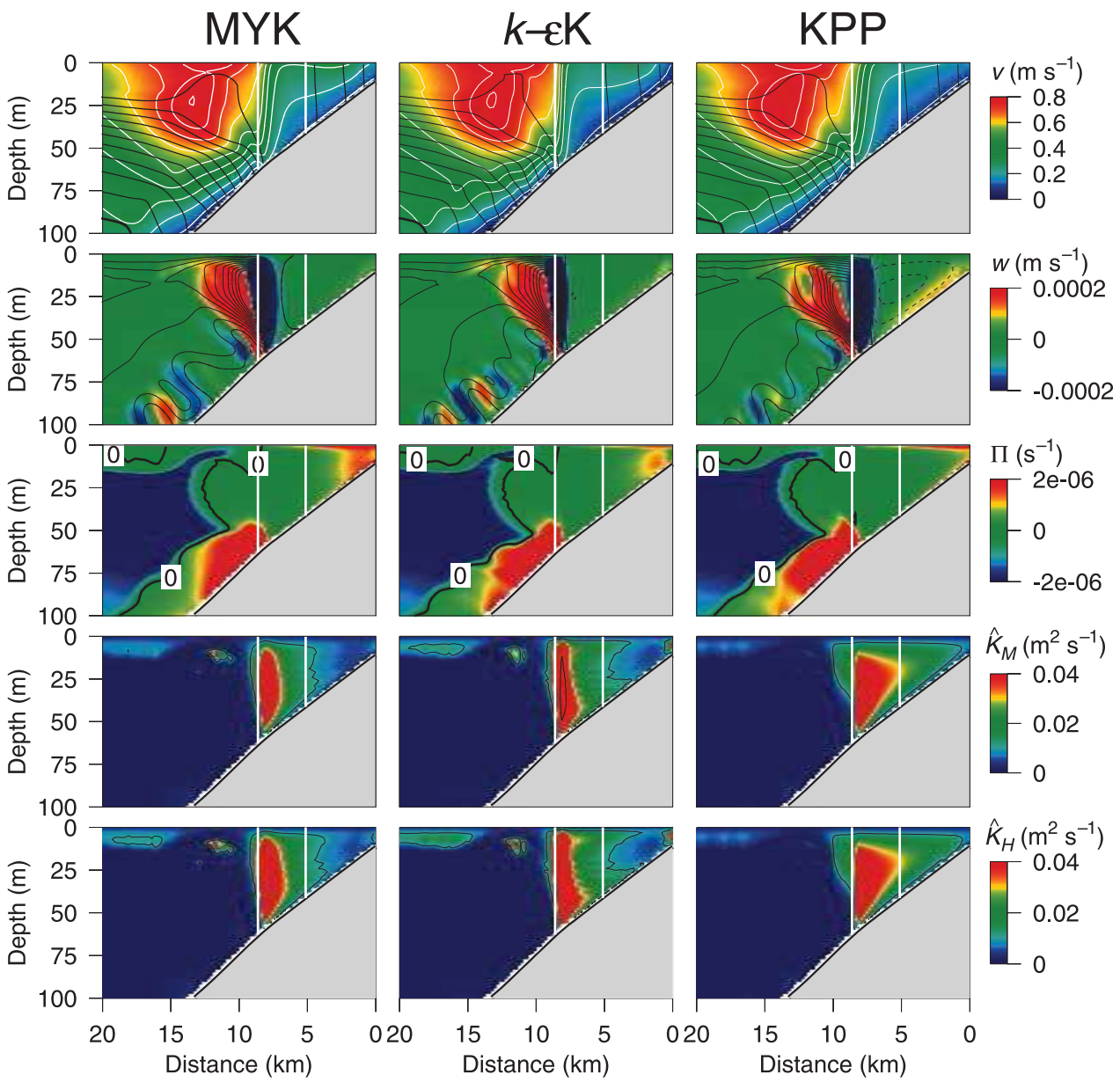

Figure 12. Fields of alongshore velocity v (color contours and white contour lines) together with density σ_θ (black contour lines), vertical velocity w (color contours) together with stream function for the across-shelf flow Ψ (black contours), potential vorticity Π, eddy viscosity $\hat{K}_M$ and eddy diffusivity $\hat{K}_H$ for the MYK, k-εK and KPP mixing schemes at $t = 24$ IP ($\approx$ day 17) for the downwelling experiments. The contour intervals are $\Delta\sigma_\theta = 0.2$ kg m^{-3}, where $\sigma_\theta = 26$ kg m^{-3} is marked by a heavy line; $\Delta v = 0.1$ m s^{-1}; $\Delta\Psi = 0.1$ m^2 s^{-1}, where $\Psi = 0$ is marked with a heavy line and $\Psi > 0$ is dashed. The vertical white lines mark the locations of profiles to be discussed in detail.

[39] At the 63-m isobath the stratification is strong at $t = 10$ IP, which is just offshore of the maximum of the alongshore jet, and mixing is restricted to the surface layer. The differences in the velocities and the density from the three schemes are small and remain small at $t = 18$ IP when the jet maximum is just offshore of this location. The density front is located near the 63-m isobath at $t = 24$ IP as shown in Figure 12. The potential density at this location is mixed nearly to the bottom. There is onshore flow near the surface and a near bottom maximum of offshore flow which is part of the recirculation cell seen in the Ψ field of Figure 12. At this location, the large mixing associated with the front does not extend to the bottom which is within the unstable boundary layer (Figures 12 and 14). The mixing coefficients are largest for k-εK and smallest for KPP with an indication of increased mixing near the bottom for KPP.

5.2. Small-Scale Variability: Comparison of MY and k-ε

[40] Fields of TKE ($q^2/2$), computed length scale l, effective length scale $\hat{l}$ (equation (A10)) used to compute $\hat{K}_M$ and $\hat{K}_H$ (equation (A9)), and the stability functions S_M

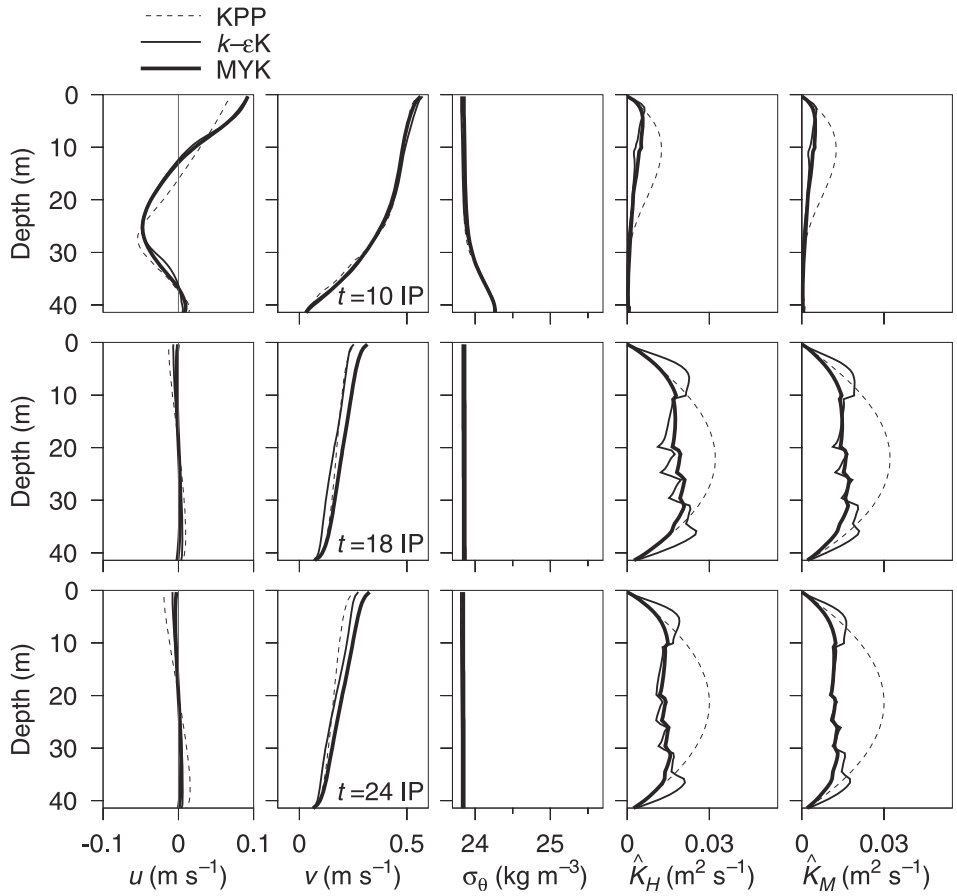

Figure 13. Vertical profiles at the 41-m isobath (5.1 km offshore) of u, v, σ_θ, $\hat{K}_H$ and $\hat{K}_M$ for t = 10 IP (≈day 7), 18 IP (≈day 15) and 24 IP (≈day 17) from the downwelling experiments. The dashed, thin and thick lines denote, respectively, the KPP, k-εK and MYK submodels.

and S_H (equation (A12)) are shown for MYK and k-εK at t = 24 IP in Figure 15. The majority of the mixing occurs in the downwelling front, surface boundary layer, and on the inner part of shelf (Figures 12–15) with some mixing in the bottom boundary layer. Qualitatively similar to the upwelling results, the *TKE* produced in the downwelling front by the k-εK scheme is substantially larger. Mixing in the interior over the midshelf is weak, where eddy viscosities and eddy diffusivities are approximately equal to the model specified background level of 2×10^{-5} m^2 s^{-1}. A striking aspect of the fields in Figure 15 is the significant difference in l and $\hat{l}$ for MYK. These differences are in sharp contrast to the close similarity of l and $\hat{l}$ found for k-εK. The values of l from MYK are evidently determined as in equation (17) from the wall proximity function. Near the bottom offshore of the front these values of l show no recognition whatsoever of the patchy nature of the *TKE* (discussed further below) associated with the symmetric instabilities. The behavior of l for MYK differs considerably from that of $\hat{l}$ and that of both l and $\hat{l}$ for k-εK. For these variables, non-zero values near the bottom reflect the patchy nature of the *TKE* distribution.

5.2.1. Downwelling Front

[41] As described above, the downwelling flow exhibits a front in both density and alongshore velocity. There is a strong circulation cell at the location of the downwelling front seen in the Ψ contours of Figure 12 with upwelling just offshore of the front. Strong mixing occurs on the shoreward side of the density front (i.e., near the bottom of the circulation cell) where vertical shear of alongshore velocity is strong and the density has either a weak stable stratification or a weak unstable stratification, depending upon the mixing scheme. *TKE*, shear production, and dissipation rate are all large near the bottom of the circulation cell (Figures 15 and 16). The major difference between MYK and k-εK mixing in the frontal region is the sign of buoyancy production term (Figure 16). MYK predicts a positive buoyancy flux on the shoreward side and a negative buoyancy flux on the offshore side of the front. Positive values of B indicate that the flow is gravitationally unstable on the shoreward side of the front and that the buoyancy production is a source of *TKE*. The k-εK scheme predicts negative values of B throughout the water column indicating that shear-driven turbulence produces *TKE* and vertical mixing.

[42] In order to look more closely at the turbulence in the frontal region, we will examine the terms in the *TKE* and q^2l equations for MYK and the *TKE* and ε equations for k-εK at t = 24 IP. The fields of the terms in the *TKE* equation are shown in Figure 16 while profiles for the terms in the *TKE*(A1), q^2l(A2) and ε (A19) equations are shown in Figure 17 at the 63-m isobath. Although P and ε are the largest terms in the *TKE* budget at the front, D_V, B, and A are

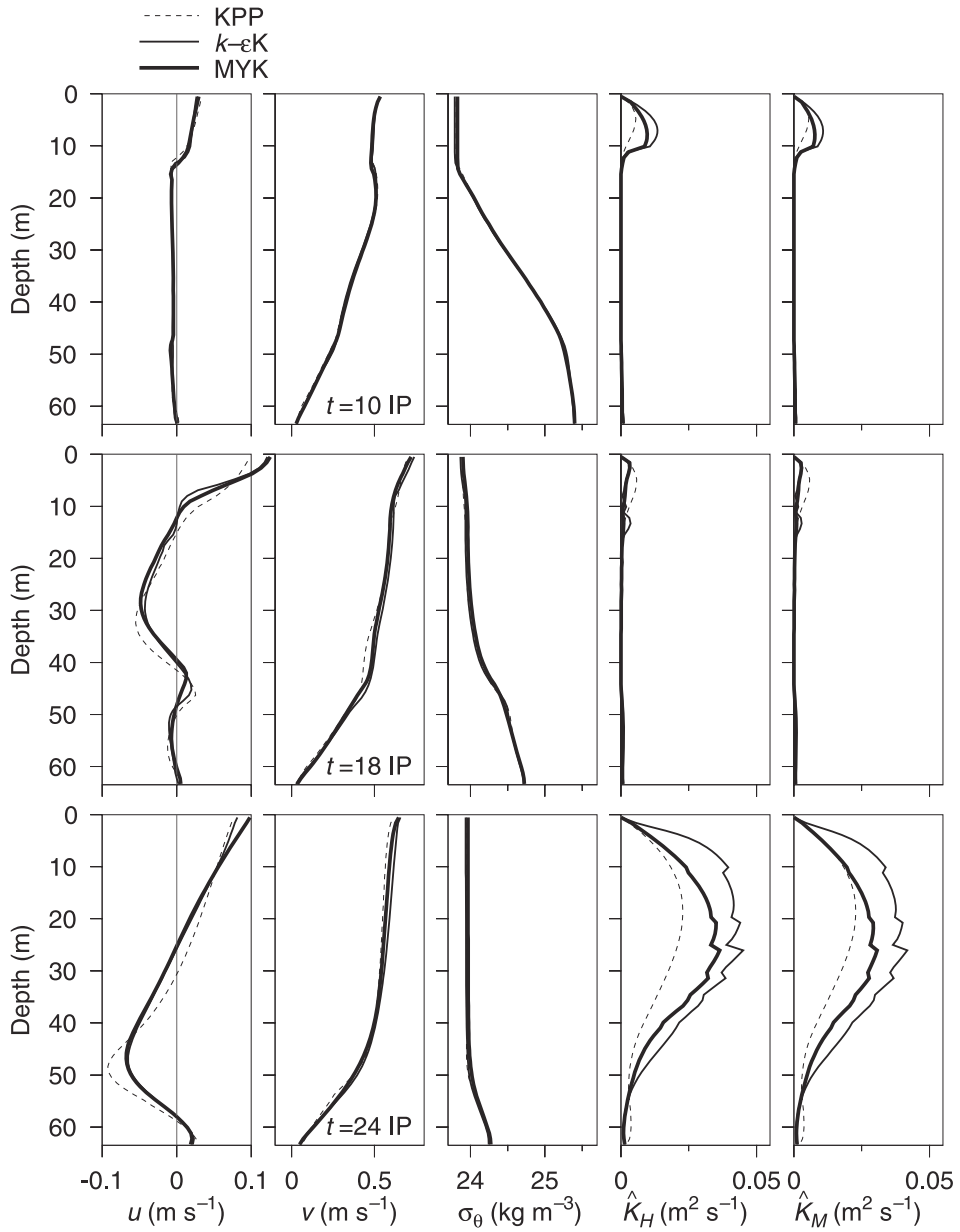

Figure 14. Vertical profiles at the 63-m isobath (8.6 km offshore) of u, v, σ_θ, $\hat{K}_H$ and $\hat{K}_M$ as in Figure 12.

essential to balance the budget (Figures 16, 17a and 17b). Vertical profiles of the q^2l and ε budgets are shown in Figures 17c and 17d. In the q^2l equation, D_{Vl}, P_l, and ε_l are in balance near the surface, while P_l, ε_l, and B_l are in balance near the bottom of the circulation cell. As during upwelling, $\varepsilon E_2(l/\kappa L)^2$ and ε provide contributions of similar magnitude to ε_l and B_l acts as a sink term (Figures 8c and 17c). In contrast, in the ε equation B_ε is a source near the bottom of the cell.

[43] Figure 18 shows profiles of the turbulence quantities *TKE*, $(q^2/2)$, l (and $\hat{l}$ dashed line), S_H, S_M, $\hat{K}_H$, $\hat{K}_M$ and ε through the region of large mixing at t = 24 IP at the 63-m isobath located about 8.5 km offshore. Results from all the versions of MY and k-ε are shown as in Figure 9. In all cases, the *TKE* has a maximum value 15–20 m above the bottom. As was seen in the upwelling case, both k-εK (Figure 9, top) and MYE (Figure 9, bottom) produce meaningful turbulent length scales l with little difference between l and $\hat{l}$ (equation (A10)). There is essentially no difference between MYK and MYG. The difference is greater between k-εK (Figure 9, top) and k-εG (Figure 9, middle) with larger values of l and bigger differences between l and $\hat{l}$ found in k-εG. At this location MYK and MYG have smaller values of *TKE* and of $\hat{K}_H$ and $\hat{K}_M$ than do the k-ε models which reflects the fact that the l produced by MYK, essentially l_{eq}^{MY} (equation (17)), is smaller than the $l_{eq}^{k\text{-}\varepsilon}$ (equation (21)). For MYO the length scale l is used in the calculation of the turbulent quantities so that there is no lower limit on G_H and therefore on S_H and S_M which are near zero in the stratified layer near the bottom resulting in a reduction of $\hat{K}_H$ and $\hat{K}_M$ in that region and in smaller values of *TKE*. Dissipation ε is large at the surface and above the bottom. As shown in Figure 16, there are large horizontal gradients in all of the terms in the equation so that distinguishing between these models on the basis of meas-

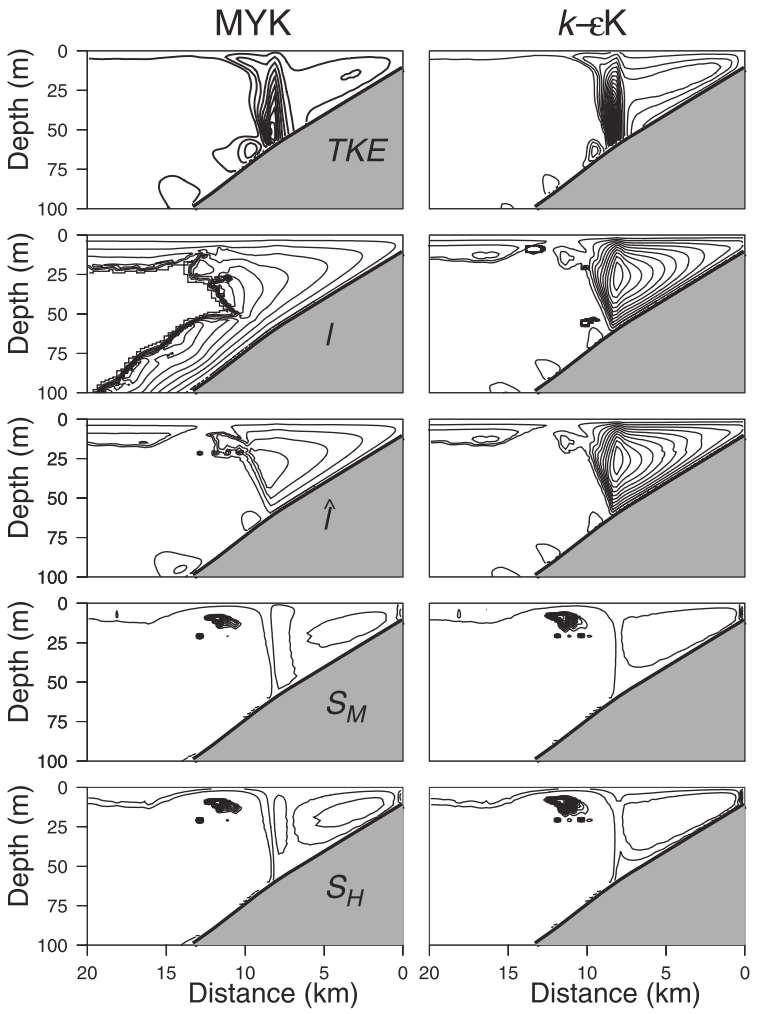

Figure 15. Fields of turbulent quantities at $t = 24$ IP from the downwelling experiment for (left) MYK and (right) k-εK. Variables include $TKE = \frac{1}{2}q^2$ (J kg^{-1}), turbulent length scale l (m), effective length scale $\hat{l}$ (m) (equation (A10)) used to calculate $\hat{K}_M$ and $\hat{K}_H$, the stability function of eddy viscosity S_M and the stability function of eddy diffusivity S_H. Contour intervals are $\Delta TKE = 2 \times 10^{-4}$, $\Delta l = \Delta\hat{l} = 1$, $\Delta S_H = \Delta S_M = 0.2$.

urements of turbulent quantities such as ε will require a very large number of closely spaced measurements.

5.2.2. Bottom Boundary Layer

[44] At $t = 24$ IP the near-bottom offshore flow produced by each turbulence scheme shows spatial oscillations in the across-shelf stream function with accompanying recirculation cells (Figures 12 and 19). *Allen and Newberger* [1996, 1998] argue that these spatially periodic oscillations are a result of finite-amplitude slantwise convection resulting from a hydrostatic symmetric instability. The strength of the vertical mixing in the bottom boundary layer also shows an oscillatory pattern similar to the stream function (Figures 12 and 19). Large values of *TKE*, dissipation rate ε, buoyancy production B, and shear production P are found in regions of offshore flow between the recirculation cells. The negative sign of buoyancy production indicates that vertical mixing is governed by shear-production. A shear-driven mixing scenario is also consistent with the idea that the boundary layer flow is susceptible to the onset of slant-wise convection without being gravitationally unstable. There are no large spatial oscillations in v and v_z, although such oscillations are clearly apparent in u and w, and their vertical derivatives. The oscillatory pattern in turbulence is therefore mainly due to the spatial variability of u_z, which is small inside recirculating cells and is large between them. It appears that the combined effects of strong shear and weak density gradients close to the bottom generate the oscillatory mixing structure shown in Figure 19.

[45] In Figure 20 we examine the near-surface alongshore velocities at $t = 24$ IP to further illustrate the differences in the mesoscale flows caused by different turbulence parameterizations. The location and magnitude of the jet are in good agreement. The largest differences are found inshore of the jet where KPP does not produce a small maximum and the magnitude of the k-εK and KPP velocities are somewhat smaller than those of MYK and MYE.

6. Summary and Conclusions

[46] The sensitivity of model-produced time-dependent upwelling and downwelling circulation on the Oregon continental shelf to the turbulent closure scheme employed

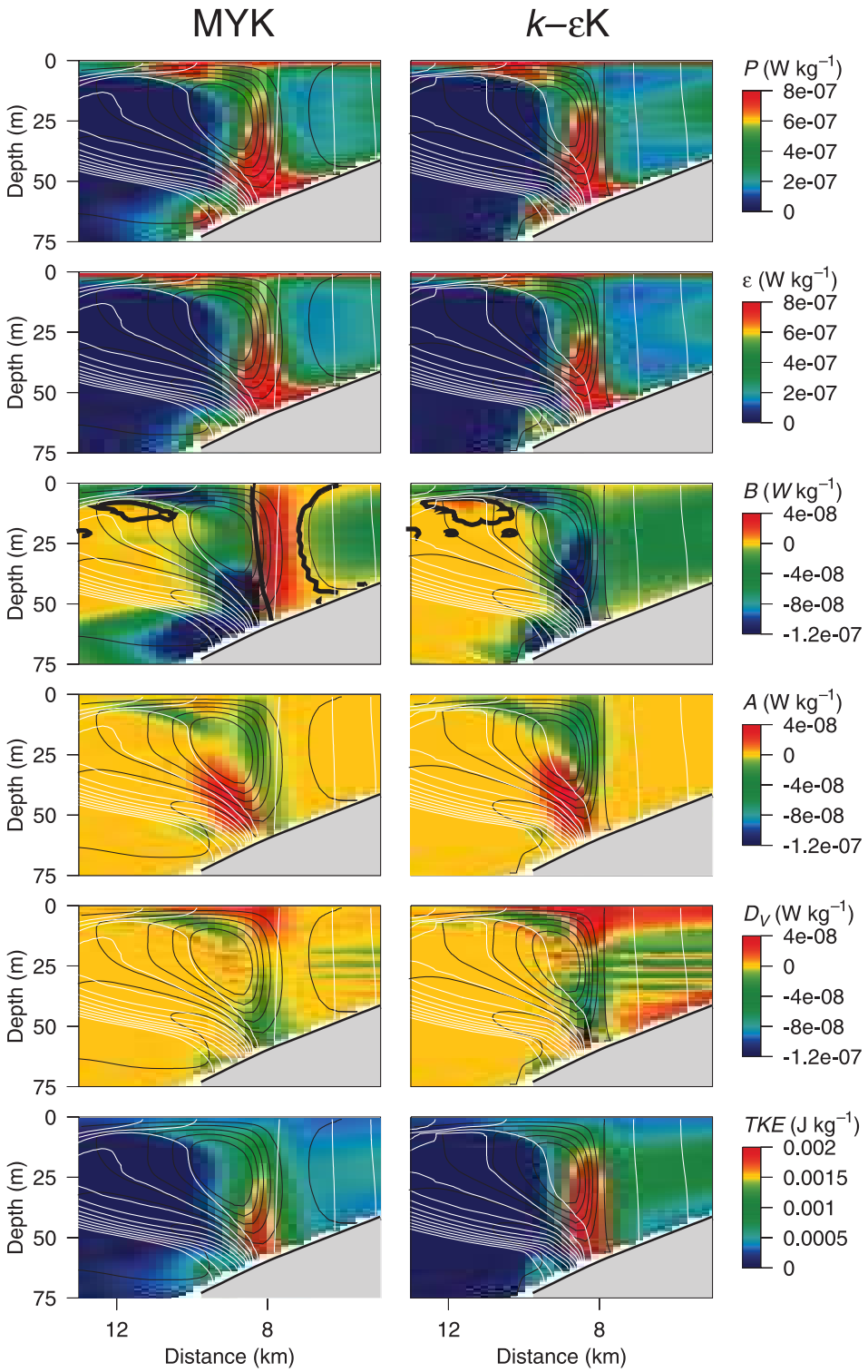

Figure 16. Mixing in the downwelling front over the inner shelf at t = 24 IP from the downwelling experiments. Color contours are shear production P, dissipation rate ε, buoyancy production B, advection A, vertical dissipation D_V and turbulent kinetic energy $TKE = \left(\frac{1}{2}q^2\right)$. The thin black lines denote Ψ, where the contour interval $\Delta\Psi = 0.1$ m^2 s^{-1}. The thin white lines are selected contours of σ_θ at the frontal boundary, where $\sigma_\theta \leq 24$ kg m^{-3} and the contour interval $\Delta\sigma_\theta = 0.05$ kg m^{-3}.

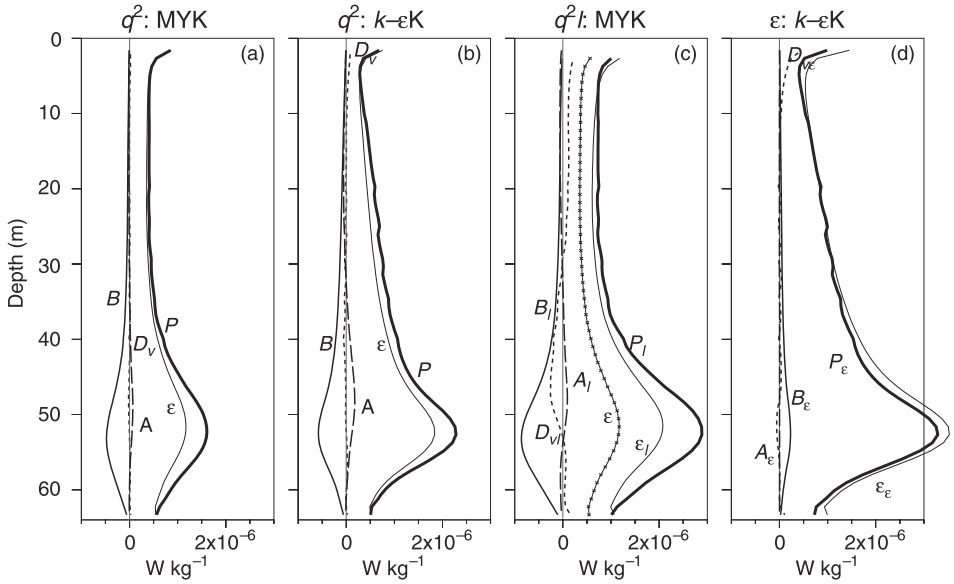

Figure 17. Vertical profiles as in Figure 8 at the 63-m isobath (8.6 km offshore) at t = 24 IP for the downwelling experiment. In addition, advection A is shown as a long dashed line. The terms in the *TKE* equation (A1) are used for (a) MYK and (b) k-εK. The terms for (c) the q^2l equation (A2) of MYK and (d) the ε equation (A19) of k-εK.

is examined using the Princeton Ocean Model [*Blumberg and Mellor*, 1987]. The level 2.5 Mellor-Yamada closure, k-ε closure, and K-Profile Parameterization schemes are used to evaluate eddy viscosities and eddy diffusivities in the circulation model. The model is forced by idealized, constant wind stress with no surface buoyancy flux. The spatial and temporal variability of mixing and the associated mesoscale fields are examined for both upwelling- and downwelling-favorable winds. Our modeling study has led to the following results.

6.1. Comparison of Submodels

[47] ● All three submodels produce similar features in the mesoscale coastal circulation. They produce qualitatively similar eddy diffusivities during both upwelling and downwelling although the turbulent structure and the mixing intensities can differ quantitatively. In particular, the predicted thickness of the surface and bottom boundaries are close for all models. This is in contrast with the earlier studies of *Allen et al.* [1995] and *Allen and Newberger* [1996] where large differences are found between results using the Mellor-Yamada closure and either constant eddy coefficients or a Richardson number mixing scheme.

[48] ● The MY and k-ε schemes provide spatial and temporal information about the turbulence quantities *TKE* and ε which are measurable. The KPP model does not.

[49] ● With the constants in equation (A12) as in the work by *Kantha and Clayson* [1994] the k-εK length-scale follows the buoyancy length scale q/N extremely well when stratification becomes important. In contrast, the length scale produced by the q^2l equation in the MYK scheme deviates substantially from the buoyancy scale during similar situations. The MYK equilibrium length scale is proportional to the length scale specified in the wall-proximity function. Inclusion in MY of the *Galperin et al.* [1988] buoyancy limitation (equation (A10)) acts to impose a dependence of the length scale on q/N. On the other hand, if in the equation for q^2l the value of the parameter E_3 is changed and is taken to be larger than 4.75, an equilibrium length scale dependent on the stratification exists and in particular with E_3 = 5.093 [*Burchard*, 2001] this model produces a turbulent length scale comparable to the buoyancy scale in stratified regions as well.

[50] ● During downwelling, the MYK scheme shows convective-mixing (positive buoyancy production) on the shoreward side of the front and shear-driven mixing (negative buoyancy production) on the offshore side. The k-εK scheme shows shear-driven mixing on both sides.

6.2. Mixing During Upwelling-Favorable Winds

[51] ● The majority of turbulent mixing occurs in the top and the bottom boundary layers, and in the vicinity of the vertically and horizontally sheared coastal jet.

[52] ● Turbulent mixing in the coastal jet is primarily driven by shear-production, which is stronger on the shoreward side of the jet than on the offshore side.

[53] ● The near-surface flow on the inner shelf becomes convectively unstable as wind stress forces the upwelled water to flow offshore in a turbulent surface layer.

6.3. Mixing During Downwelling-Favorable Winds

[54] ● The strongest mixing occurs in the vicinity of the downwelling front. The offshore side of the front is stratified and turbulent mixing is weak. The shoreward side is well mixed and turbulent mixing is strong. The largest *TKE* and ε are found near the bottom of the front.

[55] ● Turbulence in the bottom boundary layer offshore of the front is concentrated between recirculation cells which are generated as a result of symmetric instabilities in the boundary layer flow [*Allen and Newberger*, 1996]. Here *TKE* is generated by shear-production.

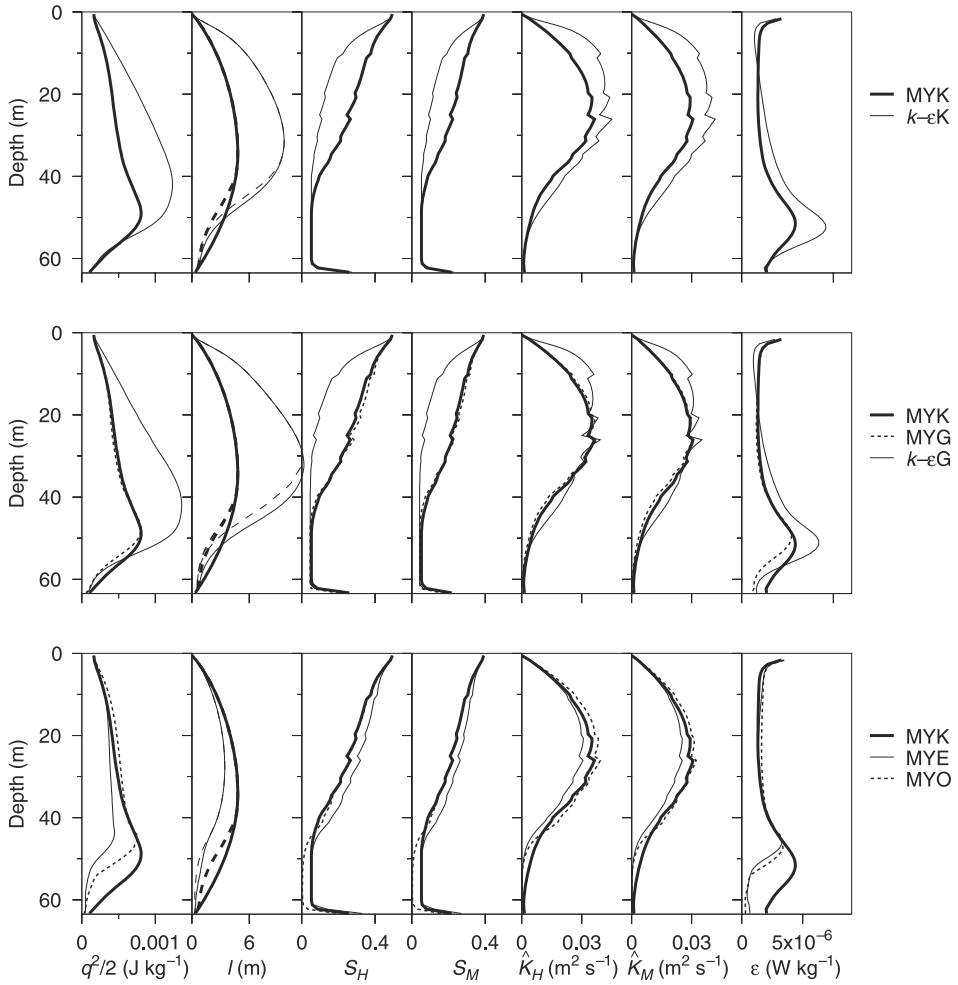

Figure 18. Vertical profiles at the 63-m isobath (8.5 km offshore) of $\frac{1}{2}q^2$, l, $\hat{l}$ (long-dashed line), S_H, S_M, $\hat{K}_H$, $\hat{K}_M$ and ε at t = 24 IP; (top) MYK and k-εK; (middle) MYK, MYG and k-εG; (bottom) MYK, MYE and MYO.

[56] Our two-dimensional mesoscale circulation study reveals interesting results concerning mixing over the Oregon shelf. Although the model experiments represent an idealized scenario (with no surface buoyancy flux and with no tides), some of the features of mixing in upwelling and downwelling fronts are captured and seem to depend only weakly on the turbulent submodel. This is notable, in particular, because of the substantial differences in model assumptions involved in the formulation of MY and k-ε compared to those used for KPP. The lack of sensitivity to the turbulence parameterization may indicate that realistic simulations are possible with the parameterizations that are in use at present. On the other hand, it also indicates that the task of comparing turbulence parameterizations with data and improving the submodels based on these comparisons will be challenging. A logical next step is to compare the submodels in a more realistic situation. Alongshore variations of all quantities, time varying forcing, surface heating and cooling and higher resolution topography will all increase the complexity of the solutions and may provide situations where the turbulence submodels behave significantly differently. It is also logical and necessary to begin to carry out detailed model-data comparisons. A major limitation in comparing model results and observations over the continental shelf is the lack of detailed turbulence and velocity measurements in the surface and bottom boundary layers and in upwelling and downwelling fronts. Since the mixing over the shelf is highly space and time dependent, measurements that resolve both space and time variability of small-scale fields are required for a meaningful comparison of model-produced mixing with observations. Necessary velocity, hydrographic, and microstructure observations over the shelf may be best obtained by combining complementary measurements from several different platforms, such as vertical profilers, towed undulating vehicles, autonomous underwater vehicles, and moored tripods. In any case, the desirability of additional observations in coastal flows that include direct measurements of turbulent quantities seems clear.

Appendix A: Turbulence Closure Schemes

A1. Mellor-Yamada Scheme

[57] To calculate eddy viscosity and diffusivity, a turbulent kinetic energy per unit mass $q^2/2$ (TKE) and a turbulent

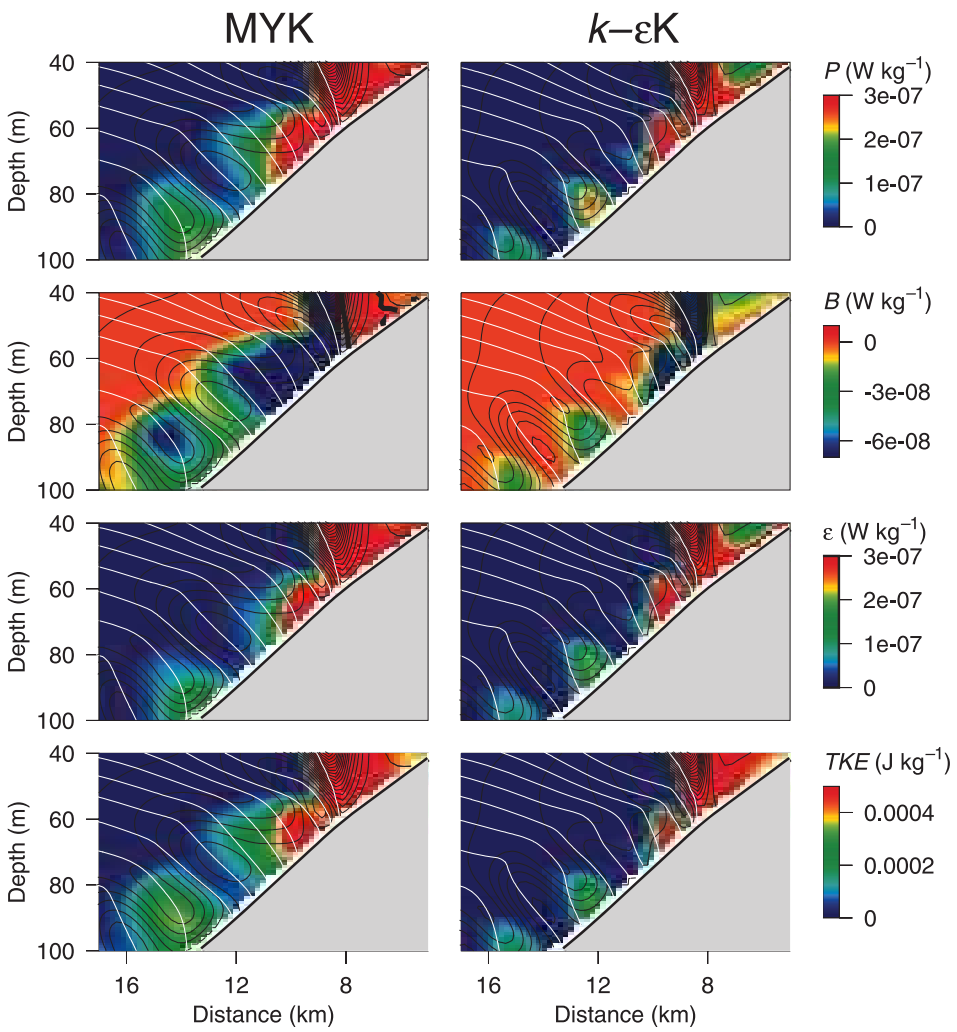

Figure 19. Mixing in the bottom boundary layer offshore of the downwelling front at t = 24 IP. Color contours are shear production P, buoyancy production B, dissipation rate ε and turbulent kinetic energy $TKE = \left(\frac{1}{2}q^2\right)$. The thin black lines denote Ψ, where the contour interval $\Delta\Psi = 0.1$ m^2 s^{-1}. The thin white lines represent selected contours of σ_θ, where $\sigma_\theta \leq 26$ kg m^{-3} and the contour interval $\Delta\sigma_\theta = 0.05$ kg m^{-3}.

length scale l are required [*Mellor and Yamada*, 1982]. The governing equations for TKE and turbulent length scale are

$$\frac{\partial(q^2D)}{\partial t}+\frac{\partial(q^2uD)}{\partial x}+\frac{\partial(q^2\omega)}{\partial\sigma}-\frac{\partial}{\partial\sigma}\left[\frac{K_Q}{D}\frac{\partial q^2}{\partial\sigma}\right]-A_H\frac{\partial}{\partial x}\left(D\frac{\partial q^2}{\partial x}\right)$$

$$=2D[P+B-\varepsilon], \tag{A1}$$

$$\frac{\partial(q^2lD)}{\partial t}+\frac{\partial(q^2luD)}{\partial x}+\frac{\partial(q^2l\omega)}{\partial\sigma}-\frac{\partial}{\partial\sigma}\left[\frac{K_Q}{D}\frac{\partial q^2l}{\partial\sigma}\right]-A_H\frac{\partial}{\partial x}\left(D\frac{\partial q^2l}{\partial x}\right)$$

$$=Dl\left[E_1P+E_3B-\hat{W}\varepsilon\right]=Dl[P_l+B_l-\varepsilon_l], \tag{A2}$$

where the shear production terms,

$$P=\frac{\hat{K}_M}{D^2}\left[\left(\frac{\partial u}{\partial\sigma}\right)^2+\left(\frac{\partial v}{\partial\sigma}\right)^2\right] \tag{A3a}$$

$$P_l=E_1P, \tag{A3b}$$

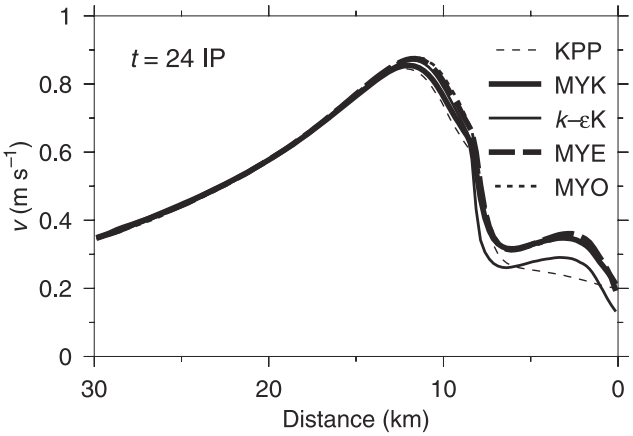

Figure 20. Near-surface alongshore velocities in the downwelling jet at t = 24 IP as a function of distance offshore from the MYK, MYE, MYO, k-εK and KPP schemes.

the buoyancy production terms,

$$B = \frac{g\hat{K}_H}{D\rho_0}\frac{\partial \sigma_\theta}{\partial \sigma} \tag{A4a}$$

$$B_l = E_3 B, \tag{A4b}$$

and the dissipation rate terms,

$$\varepsilon = \frac{q^3}{B_1 l} \tag{A5a}$$

$$\varepsilon_l = \hat{W}\varepsilon. \tag{A5b}$$

In addition, in equations (A1) and (A2) we will refer to the vertical diffusion terms as

$$D_V = \frac{1}{2D}\frac{\partial}{\partial \sigma}\left[\frac{K_Q}{D}\frac{\partial q^2}{\partial \sigma}\right] \tag{A6a}$$

$$D_{Vl} = \frac{1}{Dl}\frac{\partial}{\partial \sigma}\left[\frac{K_Q}{D}\frac{\partial q^2 l}{\partial \sigma}\right], \tag{A6b}$$

and the advection terms as

$$A = -\frac{1}{2D}\left[\frac{\partial(q^2 uD)}{\partial x} + \frac{\partial(q^2\omega)}{\partial \sigma}\right] \tag{A6c}$$

$$A_l = -\frac{1}{Dl}\left[\frac{\partial(q^2 luD)}{\partial x} + \frac{\partial(q^2 l\omega)}{\partial \sigma}\right]. \tag{A6d}$$

In equation (A2), the wall proximity function

$$\hat{W} = 1 + E_2(l/\kappa L)^2 \tag{A7a}$$

where

$$L^{-1} = (\eta - z + z_{0s})^{-1} + (H + z + z_{0b})^{-1}, \tag{A7b}$$

and z_{0s} and z_{0b} are the surface and bottom roughness lengths, respectively.

[58] The vertical diffusion coefficients are given by

$$K_Q = \hat{K}_Q + \nu_{m0}, \tag{A8a}$$

$$\hat{K}_Q = 0.41\hat{K}_M, \tag{A8b}$$

$$\hat{K}_M = q\hat{l}S_M, \tag{A9a}$$

$$\hat{K}_H = q\hat{l}S_H, \tag{A9b}$$

where ν_{m0} is constant and, following *Galperin et al.* [1988], the length scale used in calculating the vertical diffusion coefficients is given by

$$\hat{l} = \min\left(l, 0.53qN^{-1}\right) \quad \text{for } N^2 > 0 \tag{A10a}$$

$$\hat{l} = l, \quad \text{for } N^2 \le 0 \tag{A10b}$$

where N the buoyancy frequency is given by

$$N^2 = -\frac{g}{\rho_0 D}\frac{\partial \sigma_\theta}{\partial \sigma}. \tag{A11}$$

[59] The stability functions S_H and S_M, including the modifications by *Kantha and Clayson* [1994] to the functions specified by *Galperin et al.* [1988] (Table A1), are given by the solution to

$$S_H[1 - \{3A_2B_2(1 - C_3) + 18A_1A_2\}G_H] = A_2\left[1 - 6A_1B_1^{-1}\right] \tag{A12a}$$

$$S_M[1 - 9A_1A_2G_H] - S_H[9A_1\{2A_1 + A_2(1 - C_2)\}G_H] = A_1\left[1 - 6A_1B_1^{-1} - 3C_1\right], \tag{A12b}$$

where

$$G'_H = -\hat{l}^2N^2q^{-2}, \quad G_H = \min\left(G'_H, 0.028\right). \tag{A13}$$

The values of the constants used in equation (A12) are chosen following *Kantha and Clayson*, [1994] (Table A1). The stability functions of *Galperin et al.* [1988] are recovered for $C_2 = C_3 = 0$. Note that the scheme we refer to as MYK includes the *Kantha and Clayson* [1994] modifications to S_H and S_M whereas the scheme labeled MYG refers to the original *Galperin et al.* [1988] versions of S_H and S_M.

[60] The boundary conditions at the surface are

$$q^2 = B_1^{2/3}u_{\tau s}^2 \tag{A14a}$$

$$q^2 l = q^2 z_{0s} \quad \text{at} \quad \sigma = 0, \tag{A14b}$$

where

$$u_{\tau s}^2 = \left(\tau^{(x)2} + \tau^{(y)2}\right)^{1/2}/\rho_0 \tag{A15}$$

is the square of the friction velocity. The boundary conditions at the bottom are

$$q^2 = B_1^{2/3}u_{\tau b}^2 \tag{A16a}$$

$$q^2 l = q^2 z_{0b} \quad \text{at} \quad \sigma = -1, \tag{A16b}$$

where

$$u_{\tau b}^2 = \left(\tau_b^{(x)2} + \tau_b^{(y)2}\right)^{1/2}/\rho_0. \tag{A17}$$

The boundary conditions along the vertical sidewalls at the coast and offshore are

$$q_x^2 = 0 \tag{A18a}$$

$$\left(q^2 l\right)_x = 0 \quad \text{at} \quad x = 0, x_0. \tag{A18b}$$

A2. The k-ε Mixing Scheme

[61] In this scheme [e.g., *Rodi*, 1987; *Burchard et al.*, 1998], the turbulent velocity scale is estimated from the

Table A1. Coefficients Used in This Study

Experiment	A_1	A_2	B_1	B_2	C_1	C_2	C_3
MYK k-εK MYE	0.92	0.74	16.6	10.1	0.08	0.7	0.2
MYG k-εG MYO	0.92	0.74	16.6	10.1	0.08	0.0	0.0

Experiment	E_1	E_2	E_3	$c_{\varepsilon 1}$	$c_{\varepsilon 2}$	$c_{\varepsilon 3}$ stable	$c_{\varepsilon 3}$ unstable
MYK MYG MYO	1.8	1.33	1.8				
MYE	1.8	1.33	5.093				
k-εK k-εG				1.44	1.92	−0.4	1.0

TKE equation, which is identical to the q^2 equation in the MY scheme ($k = q^2/2$). The dissipation rate ε is calculated from the transport equation,

$$\frac{\partial(\varepsilon D)}{\partial t}+\frac{\partial(\varepsilon D)}{\partial x}+\frac{\partial(\varepsilon\omega)}{\partial\sigma}-\frac{\partial}{\partial\sigma}\left[\frac{K_\varepsilon}{D}\frac{\partial\varepsilon}{\partial\sigma}\right]-A_H\frac{\partial}{\partial x}\left(D\frac{\partial\varepsilon}{\partial x}\right)$$
$$=D\left(\frac{2\varepsilon}{q^2}\right)[c_{\varepsilon 1}P+c_{\varepsilon 3}B-c_{\varepsilon 2}\varepsilon]=D\left(\frac{2\varepsilon}{q^2}\right)[P_\varepsilon+B_\varepsilon-\varepsilon_\varepsilon], \tag{A19}$$

where the following quantities are defined for future use.

$$P_\varepsilon = c_{\varepsilon 1}P, \tag{A20a}$$

$$B_\varepsilon = c_{\varepsilon 3}B, \tag{A20b}$$

$$\varepsilon_\varepsilon = c_{\varepsilon 2}\varepsilon, \tag{A20c}$$

$$D_{V\varepsilon} = \frac{q^2}{2D\varepsilon}\frac{\partial}{\partial\sigma}\left[\frac{K_\varepsilon}{D}\frac{\partial\varepsilon}{\partial\sigma}\right], \tag{A21a}$$

$$A_\varepsilon = -\frac{q^2}{2D\varepsilon}\left[\frac{\partial(\varepsilon D)}{\partial x}+\frac{\partial(\varepsilon\omega)}{\partial\sigma}\right]. \tag{A21b}$$

The turbulent length scale l is obtained from ε and q^2 using equation (A5a),

$$l = \frac{q^3}{B_1\varepsilon}. \tag{A22}$$

The length scale used for calculating the vertical diffusion coefficients is $\hat{l}$ defined as for MY (equation (A10)). The constants ($c_{\varepsilon 1}$, $c_{\varepsilon 2}$) = (1.44, 1.92) [*Burchard et al.*, 1998]. For stable stratification $c_{\varepsilon 3} = -0.4$, for unstable stratification $c_{\varepsilon 3} = 1$. As in MY, $\hat{K}_Q$, $\hat{K}_H$ and $\hat{K}_M$ are obtained from equations (A8) and (A9) and $\hat{K}_\varepsilon = \hat{K}_Q/\sigma_\varepsilon$ where $\sigma_\varepsilon = 1.11$. The scheme referred to as k-εK includes the *Kantha and Clayson* [1994] functions S_H and S_M while k-εG utilizes the functions of *Galperin et al.* [1988] (Table A1).

[62] The boundary conditions for ε at the bottom and at the surface are

$$\varepsilon = \frac{q^3}{B_1\kappa(\tilde{z}+z_0)} \quad \text{as} \quad \tilde{z}\to 0, \tag{A23}$$

where $\tilde{z}$ is the distance from the bottom or the surface and z_0 is the bottom or surface roughness length. By differentiating equation (A23) with respect to $\tilde{z}$ and assuming $\partial q/\partial\tilde{z} = 0$ as $\tilde{z}\to 0$ an equivalent flux boundary condition for ε can be derived,

$$\frac{\partial\varepsilon}{\partial\tilde{z}} = -\frac{q^3}{B_1\kappa(\tilde{z}+z_0)^2} \quad \text{as} \quad \tilde{z}\to 0. \tag{A24}$$

[63] *Burchard et al.* [1998] report that high vertical gradients of ε near boundaries cause numerical problems when equation (A23) is employed and recommend the use of equation (A24). We also found numerical problems implementing boundary condition (A23) for ε and thus utilize the flux boundary condition (A24). The boundary conditions along the vertical sidewalls at the coast and offshore are

$$\varepsilon_x = 0, \quad \text{at} \quad x = 0, x_0. \tag{A25}$$

A3. K-Profile Parameterization (KPP) Scheme

[64] The KPP scheme is described in detail by *Large et al.* [1994]. Here we summarize only the main features and our implementation. In this scheme the vertical profiles of turbulent momentum and scalar fluxes for the surface and the bottom boundary layers are expressed [*Large et al.*, 1994] as

$$\overline{w\phi(z)} = -\hat{K}_\phi(\Phi_z-\gamma_\phi), \tag{A26}$$

and the corresponding profiles for the stratified interior are expressed as

$$\overline{w\phi(z)} = -\hat{K}_\phi\Phi_z, \tag{A27}$$

where Φ denotes a mean field, either a scalar or a horizontal velocity component, φ denotes fluctuations of Φ, the subscript z denotes partial differentiation and γ_ϕ is the nonlocal transport term.

[65] In the stratified interior $\hat{K}_\phi$ is a function of the gradient Richardson number Ri_g. In surface and bottom boundary layers the diffusivity $\hat{K}_\phi$ is expressed as the product of a ξ dependent turbulent velocity scale $w_\phi(\xi)$, the boundary layer height h, and a nondimensional shape function $G_\phi(\xi)$,

$$\hat{K}_\phi(\xi) = hw_\phi(\xi)G_\phi(\xi), \tag{A28}$$

where $\xi = \tilde{z}/h$, is a dimensionless vertical coordinate that varies between 0 and 1 in the boundary layer and $\tilde{z}$ is the distance from the bottom or the surface. The KPP scheme consists of determining each of these three factors for the surface and bottom boundary layers and matching the coefficients $\hat{K}_\phi$ smoothly between the boundary layers and the interior.

A3.1. Turbulent Velocity Scale

[66] The general expression for the turbulent velocity scale is

$$w_\phi = \frac{\kappa u*}{\varphi(\delta h/L_{MO})}, \delta < \xi < 1, \varsigma = \tilde{z}/L_{MO} = \xi h/L_{MO} < 0 \tag{A29a}$$

$$w_\phi = \frac{\kappa u*}{\varphi(\varsigma)} \quad \text{otherwise}, \tag{A29b}$$

where $\delta = 0.1$ is the fraction of the boundary layer where Monin-Obukhov similarity holds, ς is the stability parameter, $\varphi(\varsigma)$ is a similarity function, $L_{MO} = u_*^3/(\kappa B_f)$ is the Monin-Obukhov length with u_* the friction velocity and B_f the buoyancy flux at the boundary (for details see *Large et al.* [1994]). The surface and the bottom friction velocities are given in equations (A15) and (A17). In the case considered here, $B_f = 0$ and $w_\phi = \kappa u_*$ is independent of ξ in each boundary layer.

A3.2. Shape Function

[67] The shape function is assumed to be a cubic polynomial,

$$G_\phi(\xi) = a_0 + a_1\xi + a_2\xi^2 + a_3\xi^3. \tag{A30}$$

The four coefficients are estimated by matching the diffusivities and their vertical derivatives at $\xi = 0$ to the Monin-Obukhov similarity values and at $\xi = 1$ to the interior values. *Large et al.* [1994] obtain

$$a_0 = 0, \tag{A31a}$$

$$a_1 = 1, \tag{A31b}$$

$$a_2 = -2 + 3G_\phi(1) - G_{\phi\xi}(1), \tag{A31c}$$

$$a_3 = 1 - 2G_\phi(1) + G_{\phi_\xi}(1), \tag{A31d}$$

where

$$G_\phi(1) = \frac{\hat{K}_\phi(h)}{h w_\phi(1)}, \tag{A32a}$$

$$G_{\phi\xi}(1) = \frac{\hat{K}_{\phi\tilde{z}}(h)}{w_\phi(1)} - \frac{\hat{K}_\phi(h) w_{\phi\xi}(1)}{h w_\phi^2(1)}, \tag{A32b}$$

$\hat{K}_\phi(h)$ is the interior diffusivity (described below) at $\tilde{z} = h$ and the subscripts ξ and $\tilde{z}$ denote partial differentiation. With $B_f = 0$, $w_{\phi\xi} = 0$ so that

$$G_{\phi\xi}(1) = \frac{\hat{K}_{\phi\tilde{z}}(h)}{w_\phi(1)}. \tag{A32c}$$

A3.3. Height of the Boundary Layer

[68] The height of the boundary layer h is determined from the bulk Richardson number criterion. That is, h is equated to the smallest value of $\tilde{z}$ at which the bulk Richardson number $Ri_b(\tilde{z})$ equals a critical value of Ri_c (= 0.3), where

$$Ri_b(\tilde{z}) = \frac{\left|\tilde{B}_r - \tilde{B}(\tilde{z})\right|\tilde{z}}{|V_r - V(\tilde{z})|^2 + V_s^2(\tilde{z})}, \tag{A33}$$

V_r is the mean near-boundary reference velocity, $\tilde{B}_r$ is the near-boundary reference buoyancy, $\tilde{B}(\tilde{z}) = (g/\rho_0)\sigma_\theta(\tilde{z})$ is the buoyancy profile. The velocity scale of turbulent shear V_s is expressed as

$$V_s(\tilde{z}) = \left(\frac{C_v(-\beta_T)^{1/2}}{Ri_c\kappa^2}(c_s\delta)^{-1/2}\tilde{z}w_\phi\right)^{1/2}, \tag{A34}$$

where $C_v = 1.5$, $c_s = 93.5$ and $\beta_T = -0.2$.

[69] With stable forcing, i.e., with surface buoyancy flux upward, and $L_{MO} > 0$, the boundary layer depth is required to be less than or equal to the Monin-Obukhov length and to the Ekman depth h_e, where $h_e = 0.7u_*/f$. The requirement $h \le h_e$ is enforced for no surface buoyancy flux as well.

A3.4. Interior Diffusivity

[70] The vertical mixing in the stratified ocean interior is calculated as the superposition of three processes: local Richardson number instability due to resolved vertical shear, internal wave breaking, and double diffusion. The profile of effective interior diffusivity is written as

$$\hat{K}_\phi = K_\phi^s + K_\phi^w + K_\phi^d. \tag{A35}$$

The diffusivity due to mixing associated with shear instability K_ϕ^s is parameterized as a function of local gradient Richardson number, Ri_g,

$$K_\phi^s = K_0, \quad Ri_g < 0, \tag{A36a}$$

$$K_\phi^s = K_0\left[1 - \left(Ri_g/Ri_0\right)^2\right]^3, 0 < Ri_g < Ri_0, \tag{A36b}$$

$$K_\phi^s = 0, \quad Ri_0 < Ri_g, \tag{A36c}$$

where $K_0 = 50 \times 10^{-4}$ m^2 s^{-1}, $Ri_0 = 0.7$, and

$$Ri_g = \frac{N^2}{u_z^2 + v_z^2}. \tag{A37}$$

The coefficient K_ϕ^w is the diffusivity due to internal wave breaking, and is typically treated as a constant. Here we set $K_\phi^w = \nu_m$ for the velocity field and $K_\phi^w = \nu_h$ for the scalar field. K_ϕ^d is the diffusivity due to double diffusion, which we do not consider here and thus set $K_\phi^d = 0$.

A3.5. Calculating $\hat{K}_\phi$

[71] First, $\hat{K}_\phi$ is computed for the entire domain using the Ri_g-based criterion (A36). Boundary layer heights for the surface and bottom boundary layers at a given location are estimated from equation (A33) and turbulent velocity scales are estimated from equation (A29). If top and bottom boundary layers do not overlap, a profile of $\hat{K}_\phi$ is constructed independently for each of the boundary layers by matching $\hat{K}_\phi$ and its vertical gradients with the stratified interior (equation (A32)). In situations when the top and bottom boundary layers merge, for example, in shallow depths as wind forcing continues, we utilize the following procedure [*Durski*, 2001]. The profile of $\hat{K}_\phi$ for the surface boundary layer is calculated and matched to the Ri_g based

interior values as before. The bottom layer $\hat{K}_\phi$ and its vertical gradient are matched with the surface boundary layer values at $\tilde{z} = h$, the bottom layer height. If either boundary layer height is equal to the water depth, the profile of $\hat{K}_\phi$ is obtained by matching $\hat{K}_\phi$ and its vertical gradient to wall values at both boundaries.

Appendix B: Mellor-Yamada Equilibrium Length Scale ($E_3 \neq E_1$)

[72] We examine the equilibrium length scale l_{eq} in the MY scheme when $E_3 \neq E_1$ [*Burchard*, 2001] with the wall-proximity function (A7) included. In that case, equations (A1) and (A2) reduce to

$$P + B - \varepsilon = 0 \tag{B1}$$

$$E_1 P + E_3 B - \hat{W}\varepsilon = 0. \tag{B2}$$

[73] Utilizing equations (A4a), (A5a) and (A12) in equations (A1) and (A2) and defining

$$l_*^2 = l_{eq}^2 N^2/q^2, \tag{B3}$$

$$F_1 = \left(q^2/N^2\right)(\kappa L)^{-2}, \tag{B4}$$

$$K_1 = 3A_2B_2(1 - C_3) + 18A_1A_2, \tag{B5}$$

$$K_2 = A_2\left(1 - 6A_1B_1^{-1}\right), \tag{B6}$$

we obtain the following quadratic equation in l_*^2:

$$l_*^4 E_2F_1K_1 + l_*^2[K_2(E_3 - E_1)B_1 - (E_1 - 1)K_1 + E_2F_1]$$

$$-(E_1 - 1) = 0. \tag{B7}$$

Although the full solution to equation (B7) for l_*^2 is readily written down, it is more informative to examine the solution in limiting cases.

[74] For $F_1 \gg 1$, near the boundary where $\kappa L \ll q/N$, we obtain

$$l_{eq}^2 \sim \frac{(E_1 - 1)\kappa^2 L^2}{E_2}, \tag{B8}$$

as in equation (17). For $F_1 \ll 1$, away from the boundary where $\kappa L \gg q/N$, we obtain

$$l_{eq}^2 \sim \frac{q^2}{N^2}\frac{(E_1 - 1)}{[K_2(E_3 - E_1)B_1 - (E_1 - 1)K_1]}. \tag{B9}$$

If we follow *Burchard* [2001] and obtain an estimate for E_3 by using equation (B9) and setting

$$l_{eq} = l_{\lim} = 0.53q/N, \tag{B10}$$

where $l_{\lim}$, which motivated equation (A10a), is given by *Galperin et al.* [1988], we obtain

$$E_3 = 5.093. \tag{B11}$$

That value of E_3 is utilized in the additional experiment MYE in section 3 with $E_3 \neq E_1$. Note also from equation (B9) that to ensure $l_{eq}^2 > 0$ with $E_1 = 1.8$, it is necessary that

$$E_3 > E_{3c} = \frac{(E_1 - 1)K_1}{K_2B_1} + E_1. \tag{B12}$$

Using the constants in Appendix A, we find

$$E_{3c} = 4.75. \tag{B13}$$

[75] **Acknowledgments.** This research was supported by the National Oceanographic Partnership Program (NOPP) through ONR grant N00014-98-1-0787. Support was also provided for H.W.W. by the Office of Naval Research (ONR) Ocean Modeling and Prediction Program through grant N00014-98-1-0113 and for J.S.A. and P.A.N. by the ONR Coastal Dynamics Program through grants N00014-93-1-1301 and N00014-02-1-0100. We thank Lakshmi Kantha and an anonymous reviewer for helpful comments.

References

Allen, J. S., and P. A. Newberger, Downwelling circulation on the Oregon continental shelf: I. Response to idealized forcing, *J. Phys. Oceanogr.*, *26*, 2011–2035, 1996.

Allen, J. S., and P. A. Newberger, On symmetric instabilities in oceanic bottom boundary layers, *J. Phys. Oceanogr.*, *28*, 1131–1151, 1998.

Allen, J. S., P. A. Newberger, and J. Federiuk, Upwelling circulation on the Oregon continental shelf: I: Response to idealized forcing, *J. Phys. Oceanogr.*, *25*, 1843–1866, 1995.

Blumberg, A. F., and G. L. Mellor, A description of a three-dimensional coastal ocean circulation model, in *Three-Dimensional Coastal Ocean Models*, *Coastal and Estuarine Sci. Ser.*, vol. 4, edited by N. Heaps, pp. 1–16, AGU, Washington, D. C., 1987.

Brink, K. H., The near-surface dynamics of coastal upwelling, *Prog. Oceanogr.*, *12*, 223–257, 1983.

Burchard, H., On the the q^2l equation by Mellor and Yamada (1982), *J. Phys. Oceanogr.*, *31*, 1377–1387, 2001.

Burchard, H., O. Petersen, and T. P. Rippeth, Comparing the performance of the Mellor-Yamada and the k–ε two-equation closure models, *J. Geophys. Res.*, *103*, 10,543–10,554, 1998.

Burgett, R. L., D. Hebert, and N. S. Oakey, Vertical structure of turbulence on the southern flank of Georges Bank, *J. Geophys. Res.*, *106*, 22,545–22,558, 2001.

Dillon, T. M., Vertical Overturns: A Comparison of Thorpe and Ozmidov scales, *J. Geophys. Res.*, *87*, 9601–9613, 1982.

Durski, S. M., Physical-biological interactions in the ocean: Modeling the effects of large and small scale circulation on simple planktonic systems, Ph.D thesis, Rutgers Univ., New Brunswick, N. J., 2001.

Federiuk, J., and J. S. Allen, Upwelling circulation on the continental shelf: II. Simulations and comparisons with observations, *J. Phys. Oceanogr.*, *25*, 1867–1889, 1995.

Galperin, B., L. H. Kantha, S. Hassid, and A. Rosati, A quasi-equilibrium turbulent energy model for geophysical flows, *J. Atmos. Sci.*, *45*, 55–62, 1988.

Huyer, A., Coastal upwelling in the California current system, *Prog. Oceanogr.*, *12*, 259–284, 1983.

Kantha, L. H., and C. A. Clayson, An improved mixed layer model for geophysical applications, *J. Geophys. Res.*, *99*, 25,235–25,266, 1994.

Large, W. G., J. C. McWilliams, and S. C. Doney, Oceanic vertical mixing: A review and a model with a nonlocal boundary layer parameterization, *Rev. Geophys.*, *32*, 363–403, 1994.

Lu, Y., R. G. Lueck, and D. Huang, Turbulence characteristics in a tidal channel, *J. Phys. Oceanogr.*, *30*, 855–867, 2000.

Mellor, G. L., and T. Yamada, Development of a turbulent closure models for planetary boundary layers, *J. Atmos. Sci.*, *31*, 1791–1806, 1982.

Oke, P. R., J. S. Allen, R. N. Miller, G. D. Egbert, J. A. Austin, J. A. Barth, T. J. Boyd, P. M. Kosro, and M. D. Levine, A modeling study of the three-dimensional continental shelf circulation off Oregon: I. Model-data comparisons, *J. Phys. Oceanogr.*, *32*, 1360–1382, 2002a.

Oke, P. R., J. S. Allen, R. N. Miller, and G. D. Egbert, A modeling study of the three-dimensional continental shelf circulation off Oregon: II. Dynamical analysis, *J. Phys. Oceanogr.*, *32*, 1383–1403, 2002b.

Osborn, T. R., Estimates of the local rate of vertical diffusion from dissipation measurements, *J. Phys. Oceanogr.*, *10*, 83–89, 1980.

Ozmidov, R. V., On the turbulent exchange in a stably stratified ocean, *Izv. Acad. Sci. USSR Atmos. Oceanic Phys., Engl. Transl.*, *1*, 853–860, 1965.

Peters, H., and R. Bokhorst, Microstructure observations of turbulent mixing in a partially mixed estuary: I. Dissipation rate, *J. Phys. Oceanogr.*, *30*, 1232–1244, 2000.

Rodi, W., Examples of calculation methods for flow and mixing in stratified flows, *J. Geophys. Res.*, *92*, 5305–5328, 1987.

Rohr, J. J., E. C. Itsweire, K. N. Helland, and C. W. Van Atta, Growth and decay of turbulence in a stably stratified shear flow, *J. Fluid Mech.*, *195*, 77–111, 1988.

Simpson, J. H., W. R. Crawford, T. P. Rippeth, A. R. Campbell, and J. V. S. Cheok, The vertical structure of turbulent dissipation in shelf seas, *J. Phys. Oceanogr.*, *26*, 1579–1590, 1996.

Stacey, M. T., S. G. Monismith, and J. R. Burau, Observations of turbulence in a partially stratified estuary, *J. Phys. Oceanogr.*, *29*, 1950–1970, 1999.

Thorpe, S. A., Turbulence and mixing in a Scottish Loch, *Philos. Trans. R. Soc. London, Ser. A*, *286*, 125–181, 1977.

J. S. Allen, P. A. Newberger, and H. W. Wijesekera, College of Oceanic and Atmospheric Sciences, Oregon State University, 104 Ocean Administration Building, Corvallis, OR 97331-5503, USA. (jallen@coas.oregonstate.edu; newberg@coas.oregonstate.edu; hemantha@coas.oregonstate.edu)